



Hierarchical regulation of the resting and activated T cell epigenome by major transcription factor families

Yi Zhong^{1,2,3}, Sarah K. Walker^{4,5}, Yuri Pritykin^{1,4,6}, Christina S. Leslie^{1,2}, Alexander Y. Rudensky^{1,8}✉ and Joris van der Veeken^{1,7,8}✉

Tcell activation, a key early event in the adaptive immune response, is subject to elaborate transcriptional control. In the present study, we examined how the activities of eight major transcription factor (TF) families are integrated to shape the epigenome of naive and activated CD4 and CD8 T cells. By leveraging extensive polymorphisms in evolutionarily divergent mice, we identified the 'heavy lifters' positively influencing chromatin accessibility. Members of Ets, Runx and TCF/Lef TF families occupied the vast majority of accessible chromatin regions, acting as 'housekeepers', 'universal amplifiers' and 'placeholders', respectively, at sites that maintained or gained accessibility upon T cell activation. In addition, a small subset of strongly induced immune response genes displayed a noncanonical TF recruitment pattern. Our study provides a key resource and foundation for the understanding of transcriptional and epigenetic regulation in T cells and offers a new perspective on the hierarchical interactions between critical TFs.

Tlymphocytes are the principal cellular effectors and regulators of vertebrate immunity, critical for protection against infectious agents. Activated T cells undergo rapid proliferation and acquire specialized effector functions that allow migration to sites of infection, recruitment and stimulation of other immune cells, or direct killing of infected cells. After pathogen clearance, the activated T cell pool contracts, leaving behind a clonally expanded population of long-lived memory T cells that retain specialized features acquired during their activation¹.

Activated T cells can differentiate into distinct types of effector cells with divergent functional characteristics tailored for protection against different types of microbial and abiotic challenges^{1,2}. In addition, chronic antigen stimulation can result in a particular activation state known as dysfunction or exhaustion³, whereas local environments can invoke further distinctive features in tissue-resident T cells^{4,5}. Thus, T cells can acquire a wide range of functional states that probably represent variations on a core program executed through elaborate transcriptional regulation.

The gene expression state of a cell is primarily determined by TFs that bind to specific DNA-sequence motifs and tune the transcriptional output of the associated genes by promoting or opposing the recruitment and activity of RNA polymerase. Human and mouse genomes encode ~1,400 TFs, which can be subdivided into families based on structural similarity in their DNA-binding domains^{6,7}. TF families may contain many members capable of binding similar DNA-sequence motifs^{8,9}. TFs extensively interact with each other to combinatorially regulate transcription¹⁰. Their activity frequently relies on the recruitment of cofactors that lack sequence-specific, DNA-binding capacity, but can modify chromatin to influence its accessibility to other nuclear factors^{11,12}.

The epigenetic and transcriptional changes underlying T cell activation are driven by the concerted activity of many TFs. Although dozens of nonredundant, functionally important TFs have been identified, the regulatory logic underlying their coordinated activity is poorly understood^{2,13,14}. It is still to a large degree unclear which TFs act as activators versus repressors, and which TFs have more general versus more specialized functions in defining T cell activation states. Moreover, although many pairs of TFs have been shown to bind to overlapping sets of targets, the importance of these interactions is largely unknown.

To gain new insights into the transcriptional regulation of T cell activation states, we have leveraged naturally occurring polymorphisms in TF-binding motifs in mice^{15,16}. The wild-derived inbred strain Cast/Eij (Cast) has roughly 20 million genetic variants relative to the C57BL/6 (B6) strain, many of which overlap with *cis*-regulatory elements¹⁶. By linking these polymorphisms to allelic imbalances in transcription, chromatin accessibility, TF and cofactor binding in (B6/Cast) F1 mice, we have dissected the mechanisms underlying transcriptional and epigenetic regulation in T cells undergoing activation in response to an acute viral infection. We found that positive regulation of chromatin accessibility and gene expression in naive T cells is overwhelmingly dependent on just a few TF families, including Ets, Runx and TCF/Lef. Representative members of these families occupy most accessible chromatin regions and interactions between them define distinct epigenetic responses to T cell activation. Ets1 binding defined regulatory elements overlapping with promoters of housekeeping genes, the accessibility of which was largely unchanged upon T cell activation despite the recruitment of a variety of activation-dependent TFs and cofactors. Conversely, Runx1 dynamically bound to nearly all acces-

¹Howard Hughes Medical Institute and Immunology Program, Sloan Kettering Institute and Ludwig Center at Memorial Sloan Kettering Cancer Center, New York, NY, USA. ²Computational and Systems Biology Program, Memorial Sloan Kettering Cancer Center, New York, NY, USA. ³Shanghai Immune Therapy Institute, Renji Hospital, Shanghai Jiao Tong University School of Medicine, Shanghai, China. ⁴Lewis-Sigler Institute for Integrative Genomics, Princeton University, Princeton, NJ, USA. ⁵Quantitative and Computational Biology Graduate Program, Princeton University, Princeton, NJ, USA.

⁶Department of Computer Science, Princeton University, Princeton, NJ, USA. ⁷Research Institute of Molecular Pathology, Vienna Biocenter, Vienna, Austria.

⁸These authors jointly supervised this work: Alexander Y. Rudensky, Joris van der Veeken. ✉e-mail: rudenska@mskcc.org; joris.van.der.veeken@imp.ac.at

sible chromatin regions in a manner that was strongly dependent on its own motif as well as motifs for other TFs that were induced or repressed upon T cell activation. Runx motifs positively affected the accessibility of these elements, suggesting that Runx TFs promiscuously amplify the activity of multiple TFs. Finally, TCF1 binding defined elements whose accessibility was typically lost upon T cell activation unless displaced by other activation-induced TFs. In addition to these canonical behaviors that defined most of the chromatin accessibility changes upon T cell activation, we found a small set of regulatory elements associated with immune response genes that showed a noncanonical pattern of Ets1 and TCF1 recruitment. This observation suggests that the expression of strongly induced immune response genes may be regulated in an atypical manner through the recruitment of TFs whose functions are normally dedicated to other cellular processes. Together, our study provides new insights into the relationships between TFs that regulate T cell activation.

Results

TF motifs that regulate chromatin accessibility in T cells. Although naive and activated T cells express many functionally important TFs, it is unclear which of these factors act as determinants of chromatin accessibility. To address this question, we performed assay for transposase-accessible chromatin using sequencing (ATAC-seq) on naive CD4 and CD8 T cells isolated from uninfected B6/Cast F1 mice and activated virus-specific T cells isolated on day 7 post-infection of B6/Cast F1 mice with lymphocytic choriomeningitis virus (LCMV) Armstrong, and analyzed the effects of TF-binding motif polymorphisms on allele-specific chromatin accessibility (Fig. 1a, Extended Data Fig. 1a,b and Supplementary Table 1). We identified a limited number of motifs that strongly affected chromatin accessibility (Fig. 1b and Extended Data Fig. 1c). Ets, Runx, and specific bZIP and IRF family motifs showed a strong positive association with chromatin accessibility across cell types and activation states, with Ets motifs showing the strongest association. In contrast, other motifs showed cell state-specific effects: Sox and bHLH motif variants preferentially affected chromatin accessibility in naive cells, whereas T-box and specific bZIP or bZIP-IRF4 composite (Batf) motifs had a greater effect in activated cells (Fig. 1b and Extended Data Fig. 1c).

A comparison between CD4 and CD8 T cells revealed that TF-binding motifs affecting chromatin accessibility in naive cells were very similar (Extended Data Fig. 1d). In contrast, several motifs selectively affected chromatin accessibility in activated CD4 versus CD8 T cells (Extended Data Fig. 1e). Variation in T-box motifs preferentially affected activated CD8 versus CD4 T cells, consistent with increased expression of the T-box family TFs T-bet and Eomes in the former (Extended Data Fig. 1e,f). Conversely, TCF7/Lef1 motifs preferentially affected activated CD4 versus CD8 T cells, consistent with stronger activation-induced downregulation of *Tcf7* in the latter (Extended Data Fig. 1e,f). These results suggest that a relatively limited number of TF families is responsible for driving chromatin accessibility in T cells, with some showing graded cell type and cell state-specific activity.

Although chromatin accessibility changes induced upon T cell activation were positively correlated with nearby gene expression, we also identified many individual peaks for which this association was not evident, raising the possibility that gene expression changes may be driven by TFs distinct from those affecting chromatin accessibility (Extended Data Fig. 2a). However, we found that changes in aggregated ATAC-seq counts from multiple peaks linked to the same gene were almost always associated with gene expression changes, with the exception of a small subset of cell cycle-related genes with transient modulation that was uncoupled from chromatin accessibility changes (Extended Data Fig. 2b,c). Thus, most gene expression changes are strongly associated with cumulative

accessibility changes across regulatory elements within a locus. Consistently, we found that TF-binding motif polymorphisms affecting chromatin accessibility typically also affected nearby gene expression to varying degrees (Fig. 1c). Together, these observations suggest that, under our study conditions, most gene expression and chromatin accessibility changes are driven by the same core set of sequence-specific TFs.

Although some motifs implicated in activation-induced chromatin remodeling were also identified through conventional motif enrichment analysis, others were identified only by allele-specific analysis, including the naive T cell-specific activity of certain bHLH motifs (Fig. 1d). Moreover, conventional motif enrichment analysis was unable to distinguish between activating and repressive activity. For example, although both Batf and Pou2f2 motifs were enriched among peaks gaining accessibility upon T cell activation, allele-specific analysis suggested that the former acted as a strong activator selectively in activated cells, whereas the latter acted as a weak repressor in naive cells (Fig. 1e). Thus, the effects of genetic variation provided new insights into chromatin regulation.

Ets1, Runx1 and TCF1 occupy most of the accessible genome. We next sought to characterize the interplay between TFs with binding motifs implicated in regulating chromatin accessibility. We first characterized binding of TFs with motifs that were most strongly linked to chromatin accessibility in naive T cells. Analysis of Ets1, Runx1 and TCF1 binding by CUT&RUN revealed many TF-occupied sites covering ~93.6% of the accessible genome in naive T cells (Fig. 2a,b and Extended Data Fig. 3a,b). Ets1-, Runx1- and TCF1-bound sites extensively overlapped, with ~51.4% of sites bound by all three factors. Strikingly, these ‘triple occupied’ sites accounted for almost all (86.8%) Ets1-bound elements, which were strongly enriched for promoters and first exons of genes (Fig. 2c). Smaller subsets of sites were bound by both Runx1 and TCF1 (22.9%), or Runx1 alone (8.1%) (Fig. 2b). Thus, most accessible chromatin regions in naive T cells are occupied by some combination of Ets1, Runx1 and TCF1.

The observation that Ets1-bound sites were typically co-occupied by all three TFs raised the possibility that these elements were bound nonspecifically. To determine whether TF binding to these regions was motif dependent, we assessed the effects of motif polymorphisms on allele-specific TF occupancy at Ets1-bound sites. We found that binding of all three TFs was modulated by polymorphisms in their respective TF-binding motifs (Fig. 2d). Thus, Runx1, TCF1 and Ets1 binding were dependent on intact Runx, Sox and Ets motifs, respectively. In addition, binding of Runx1 and TCF1 were strongly affected by variation in Ets motifs (Fig. 2d and Extended Data Fig. 3c). Thus, TF binding to shared targets was motif dependent and most likely specific. Moreover, Ets motifs, which act as the strongest determinants of chromatin accessibility, enhanced the binding of other TFs at shared targets.

Importantly, chromatin accessibility of Ets1-bound sites was to a large degree identical across naive and activated CD4 and CD8 T cells (Fig. 2e). Conversely, sites bound by Runx1 or TCF1 in the absence of Ets1 underwent widespread activation-induced chromatin remodeling and showed frequent differential accessibility (Fig. 2e). Accordingly, genes near Ets1-bound chromatin regions were constitutively expressed at high levels and enriched for genes involved in metabolic processes, whereas genes associated with Runx1- or TCF1-bound regions not co-occupied by Ets1 were differentially expressed between cell types and enriched for genes involved in a variety of processes, including localization, cellular communication and leukocyte activation (Fig. 2f and Extended Data Fig. 3d,e). Thus, Ets1 binding defines a set of constitutively accessible genetic elements associated with housekeeping genes, which are typically co-occupied by Runx1 and TCF1 and account for more than half of the accessible genome in naive T cells.

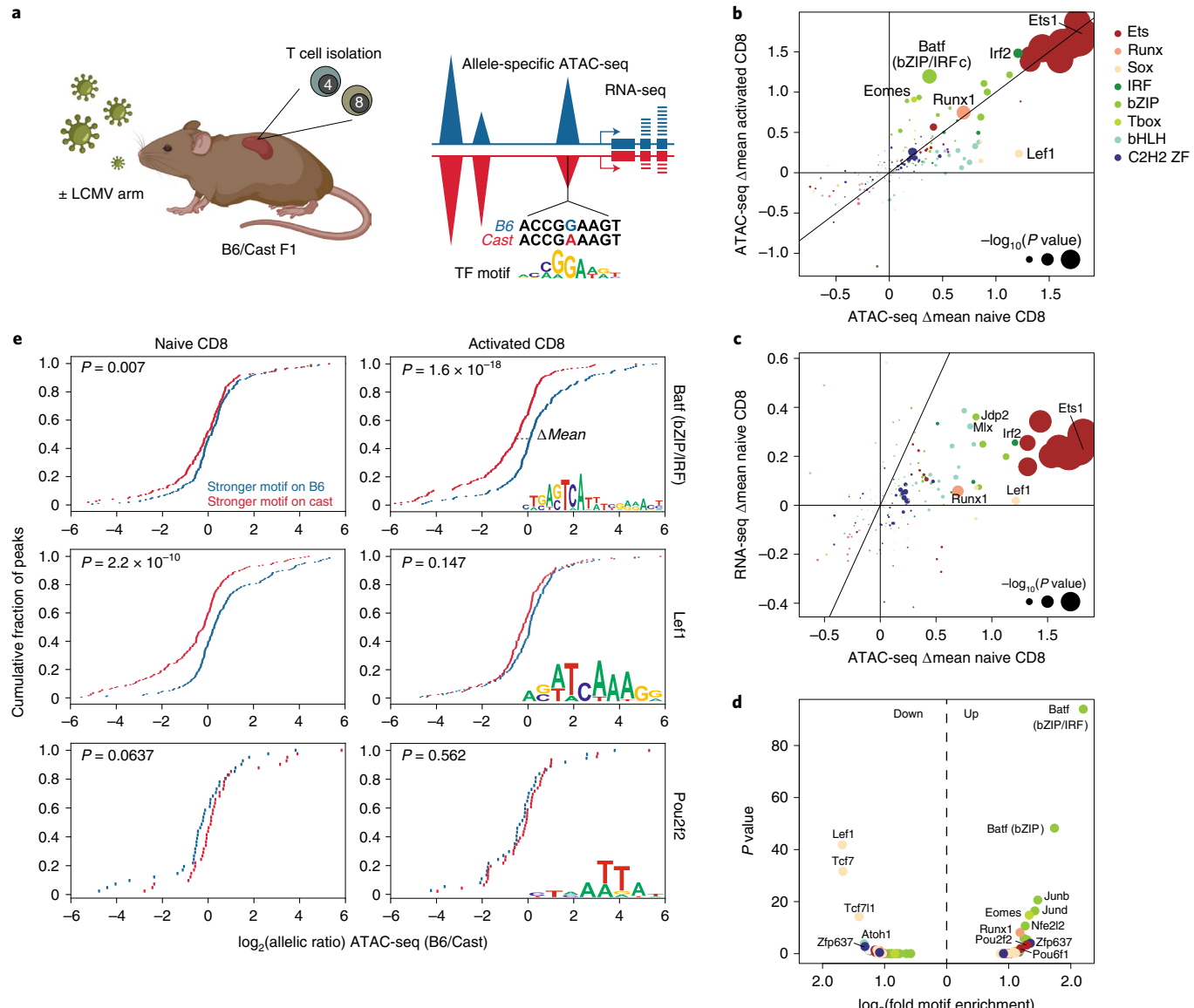


Fig. 1 | Effect of TF-binding motif polymorphisms on allele-specific chromatin accessibility in naive and activated T cells. **a**, Experimental schematic. F1 (B6/Cast) mice were infected with 2×10^5 p.f.u. of LCMV Armstrong injected intraperitoneally or left uninfected. LCMV-specific CD4 and CD8 T cells were isolated on day 7 post-infection based on staining with I-A^b LCMV GP66-77 and H-2D^b LCMV NP396-404 tetramers, respectively. Naive CD44^{lo}CD62L^{hi}TCR β ⁺ CD4 and CD8 T cells were isolated from uninfected mice. Sorted cell populations were subject to allele-specific ATAC-seq and RNA-seq analysis. Sequencing reads were aligned to a pseudo-diploid B6/Cast genome. Reads were counted as B6 or Cast specific depending on the better genome alignment. After summing up all variant-containing reads across the gene or peak region, the allelic ratio of RNA-seq or ATAC-seq signal was calculated as B6-specific reads/Cast-specific reads. Peaks overlapping with variant-containing TF-binding motifs (TF motif) were divided into those containing stronger matches on the B6 allele and those containing stronger matches on the Cast allele. The mean allelic ratios of these two peak sets were compared using a Student's *t*-test. The difference in mean allelic ratio between the two peak sets is denoted as ΔMean . This is further illustrated in **e**. The figure was created with BioRender.com. **b**, Effect of TF-binding motif variants on chromatin accessibility measured as ΔMean in naive and activated CD8 T cells. Data points are colored by TF family and scaled according to the $-\log_{10}(P \text{ value})$ of a Student's *t*-test comparing the mean allelic ratios of peak sets with stronger matches on the B6 versus the Cast allele. The most significant *P* value obtained across the two cell types (naive and activated CD8) was used for scaling. Variant-containing motifs with <50 occurrences throughout the genome were excluded from the plot. **c**, Effect of TF-binding motif variants on chromatin accessibility and gene expression in naive CD8 T cells. To determine the effect of motif variants on allelic bias in gene expression, peaks were linked to the nearest gene. **d**, TF-binding motif enrichment in peaks gaining or losing chromatin accessibility (fold-change >2) compared with peaks whose accessibility was unchanged in activated versus naive CD8 T cells (Fisher's exact test, one-sided *P* values corrected by the Benjamini-Hochberg procedure). **e**, Distribution of allelic ratios in ATAC-seq counts for peaks containing variants in select TF-binding motifs. ΔMean describes the difference in mean allelic ratio between the blue peaks and the red peaks (two-sided *P* values were obtained from a Student's *t*-test for the null hypothesis that the independent allelic ratios of blue and red *cis*-elements have an identical expected value μ).

Ets1 binding defines constitutively accessible chromatin. We next sought to understand how the functions of activation-induced TFs were integrated with the pre-existing chromatin landscape.

As Ets1-bound elements did not undergo major accessibility changes in activated versus naive T cells, it was possible that TFs whose expression or activity was modulated upon T cell activa-

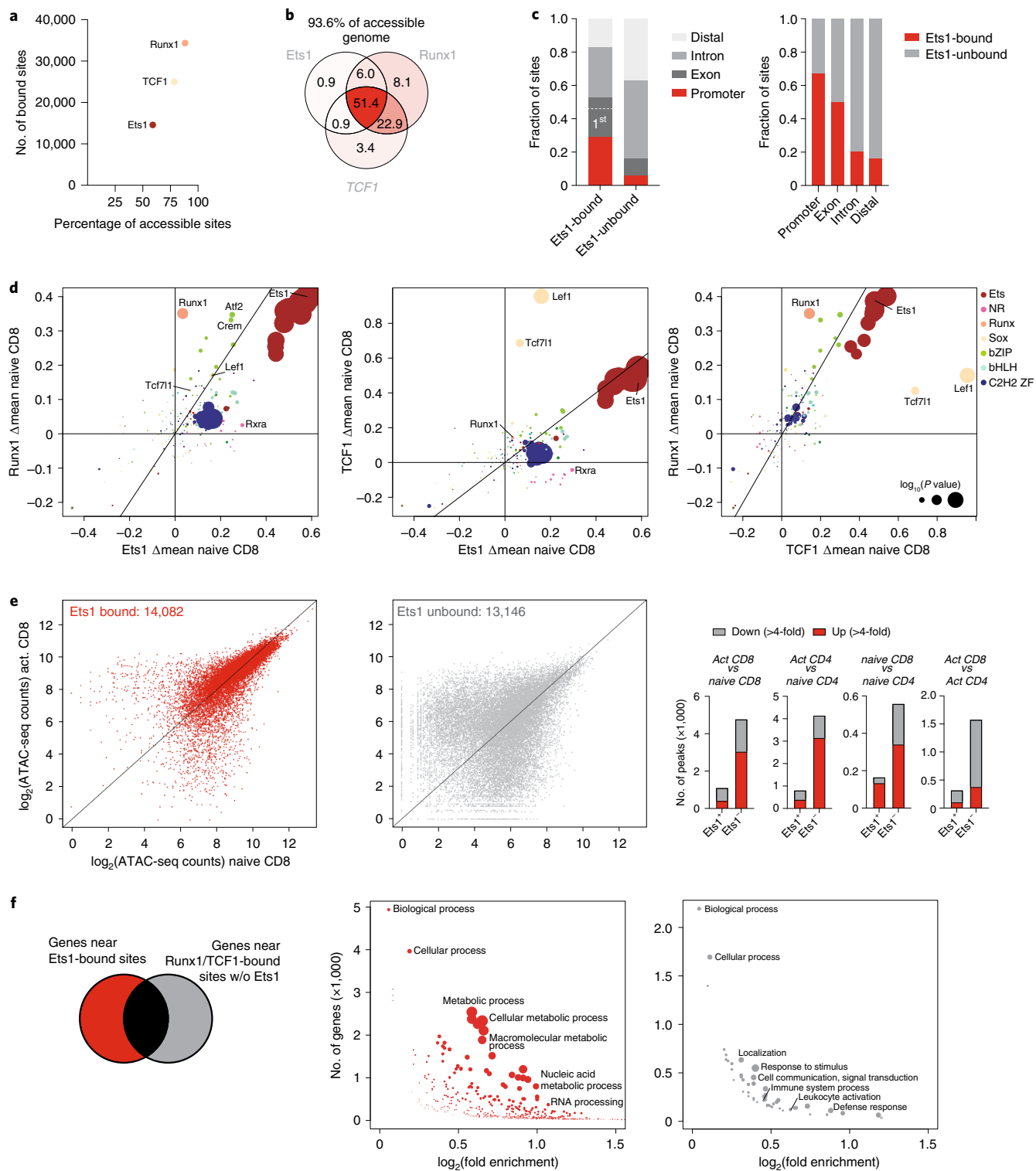


Fig. 2 | Runx1, TCF1 and Ets1 occupy most accessible chromatin regions. **a**, Runx1, TCF1 and Ets1 binding in naive CD8 T cells measured by CUT&RUN. The number of ATAC-seq peaks bound by each TF is shown, together with the fraction of all accessible peaks (>100 ATAC-seq reads in naive T cells) that is bound by each factor. **b**, The fraction of all accessible peaks (>100 ATAC-seq reads in naive T cells) that is bound by each combination of Runx1, TCF1 and Ets1. **c**, Composition of Ets1-bound and -unbound regulatory elements (left). The fraction of ATAC-seq peaks overlapping with promoters, exons, introns and distal elements bound by Ets1 (right) is shown. **d**, The effect of genetic variation in TF-binding motifs on allelic bias in Runx1, Ets1 and TCF1 binding in naive T cells. The data points are colored by TF family and scaled according to the $-\log_{10}(P \text{ value})$ of a two-sided Student's *t*-test comparing the allelic ratios between peaks with stronger matches on the B6 versus the Cast allele. **e**, Chromatin accessibility at ATAC-seq peaks bound by TCF1 or Runx1 with (Ets1 bound) or without Ets1 (Ets1 unbound) (left). The number of differentially accessible peaks (>100 reads in at least one cell type) across various comparisons (right) is shown. Act., Activated. **f**, Gene ontology (GO) term enrichment analysis of nonoverlapping genes nearest to Ets1-bound versus -unbound peak sets. w/o, without. The data points are scaled according to the false discovery rate.

tion were not recruited to these sites. To address this question, we determined the binding patterns for select representatives of bZIP, bHLH, IRF, T-box and Rel TF families in activated CD4 and CD8 T cells 7 d post-infection with LCMV Armstrong. CUT&RUN of c-Jun, Bhlhe40, IRF4, T-bet and NFATc1 revealed that each of these factors bound to ~20–50% of accessible regions in activated T cells (Fig. 3a,b). Interestingly, although most of the binding sites of these factors overlapped with Ets1 and underwent only minor changes in accessibility during T cell activation (Fig. 3c,d), only those that did not overlap with Ets1 binding underwent dramatic activation-induced chromatin remodeling (Fig. 3d). Thus, although activation-induced TFs are recruited to sites with and without Ets1 binding, their activity seems to be restricted selectively to the latter set of elements.

We considered the possibility that specific combinations of TFs present at sites not bound by Ets1 were responsible for driving accessibility changes. However, we found that binding sites of activation-induced TFs overlapped more extensively at Ets1-bound versus -unbound sites (Fig. 3e). At sites bound by at least one activation-induced TF, co-occupancy by all five factors was much more common than expected by chance and similarly enriched at both Ets1-bound and -unbound elements (Fig. 3f). Moreover, although certain combinations of activation-induced TFs occurred more frequently than others at Ets1-unbound sites, all combinations were associated with activation-induced increases in chromatin accessibility (Fig. 3g). In general, binding of a greater number of activation-induced TFs to Ets1-unbound elements was associated with greater changes in accessibility (Fig. 3h). Thus, differential changes in chromatin accessibility at Ets1-bound and -unbound sites induced upon T cell activation are unlikely to be accounted for by differential recruitment of activation-induced TFs.

Although we considered the possibility that activation-induced TFs were recruited to constitutively accessible Ets1-bound sites in a manner independent of their respective binding motifs, analysis of allele-specific TF occupancy was inconsistent with this idea (Fig. 3i). On the contrary, we found that, at Ets1-bound *cis*-regulatory elements, binding of each activation-induced TF was dependent on the presence of its respective TF-binding motif. In addition, binding of these TFs at Ets1-unbound elements was modulated by polymorphisms in bZIP/IRF composite (Baf) motifs. Thus, recruitment of activation-induced TFs to both pre-accessible Ets1-bound, and newly accessible Ets1-unbound, elements was motif dependent. Together, these observations suggest a simple model in which the functions of activation-induced TFs are overlaid onto the pre-existing chromatin landscape of naive T cells (Fig. 3j).

Immune response genes recruit Ets1 upon T cell activation. Although Ets1 binding was largely similar between activated and naive T cells, our analysis revealed a small subset of sites (375 or ~2.5% of Ets1-bound sites) that gained Ets1 binding upon T cell activation (Fig. 4a and Extended Data Fig. 4a). In contrast to other Ets1 targets, these elements were typically much less accessible in naive T cells and were nearest to immune response-related genes with expression strongly induced upon T cell activation (Fig. 4b,c). Although most of the constitutively bound Ets1 targets overlapped with promoters and first exons of genes, these upregulated Ets1 (Ets1^{up}) sites typically overlapped with intronic and distal regulatory elements that were almost always co-occupied by multiple activation-induced TFs (Figs. 2c and 4d,e). In contrast to most Ets1-bound sites, Ets1^{up} sites strongly gained accessibility upon T cell activation and underwent even more dramatic changes in accessibility than Ets1-unbound sites that recruited a similar number of activation-induced TFs (Fig. 4f). The observation that, despite high Ets1 expression, Ets1^{up} sites were not bound in naive T cells raised the possibility that these sites lacked canonical Ets1 motifs. Indeed,

Ets1^{up} sites were relatively depleted of intact Ets motifs and typically matched the canonical Ets motifs to a lesser degree (Fig. 4g), but were enriched for stronger bZIP (Baf) and T-box motifs compared with other Ets1-bound sites.

Another factor that could contribute to the lack of Ets1 binding to Ets1^{up} sites in naive T cells is that these ‘noncanonical’ sites require prior chromatin remodeling to render them accessible for Ets1 binding. A corollary to this model is that Ets1 alone would not be sufficient for the recruitment of the remodeling factors. To address this possibility, we analyzed the binding patterns of key subunits of four ATP-dependent chromatin remodelers—Snf2h, Chd4, Ruvbl1 and Brg1—in activated T cells¹⁷. Although Snf2h, Chd4 and Ruvbl1 were almost universally present at all TF-bound regions, binding of Brg1, the ATPase subunit of SWI/SNF (SWItch/Sucrose Non-Fermentable), was restricted to a smaller subset of sites (Fig. 4h and Extended Data Fig. 4b). We found that, at Ets1-bound and -unbound, and Ets1^{up} sites alike, the binding of increasing numbers of activation-induced TFs was associated with recruitment of Brg1 (Fig. 4i). Analysis of the effects of TF-binding motif polymorphisms on allele-specific Brg1 recruitment revealed that, in addition to Ets motifs, T-box, bZIP, IRF and bZIP/IRF composite motifs acted as major positive regulators of Brg1 recruitment (Extended Data Fig. 4c). Thus, although intact Ets motifs might contribute to its binding or retention, Brg1 is typically not recruited to sites that are bound by Ets1 in the absence of activation-induced TFs.

Together, our results suggest that Ets motifs have a dominant effect on chromatin accessibility throughout the genome. Although binding of Ets1 is typically restricted to constitutively accessible elements associated with promoters of housekeeping genes, a small subset of Ets1-bound enhancers associated with immune response-related genes recruits Ets1 upon T cell activation and undergoes dramatic chromatin remodeling. These Ets1^{up} sites contain fewer and weaker Ets motifs, and the binding of Ets1 to these sites may require assistance from other activation-induced TFs and the chromatin remodeler Brg1 (Fig. 4j).

Runx1 amplifies genome-wide chromatin accessibility changes. Our analysis suggested that, similar to Ets motifs, Runx motifs also contributed to chromatin accessibility in a largely constitutive manner (Fig. 1b). However, in contrast to Ets1, we found that Runx1 binding was detectable at nearly all accessible sites across the genome, including those gaining or losing accessibility upon T cell activation (Fig. 5a–c). Activation-induced widespread changes in Runx1 binding that correlated with chromatin accessibility changes (Fig. 5d). Thus, in contrast to Ets1, which binds mostly to constitutively accessible sites, Runx1 is redistributed upon T cell activation. This observation suggests that Runx1 is recruited to a very large fraction of its binding sites in a nonautonomous manner.

To determine the mechanisms underlying Runx1 redistribution, we analyzed the effects of TF-binding site polymorphisms on allele-specific Runx1 binding at sites strongly gaining or losing (more than fourfold) chromatin accessibility in activated versus naive T cells. We found that polymorphisms in Runx motifs, which were the most abundant motifs at these sites, strongly affected Runx1 binding in both naive and activated T cells (Fig. 5e,f). Lef1 (Sox) motifs, which were highly enriched at sites losing accessibility upon T cell activation, selectively affected Runx1 binding in naive T cells. Conversely, bZIP and T-box motifs, enriched at sites that gained accessibility, selectively affected Runx1 occupancy in activated T cells. These results suggest that distinct TFs contribute to Runx1 localization in naive and activated T cells. Importantly, we found that polymorphisms in Runx motifs affected the accessibility of these activation-dependent Runx1 targets, suggesting that Runx1 is not just passively recruited to all accessible sites, but actively contributes to increasing chromatin accessibility (Fig. 5g). Based on these observations, we propose that Runx TFs may act as promiscu-

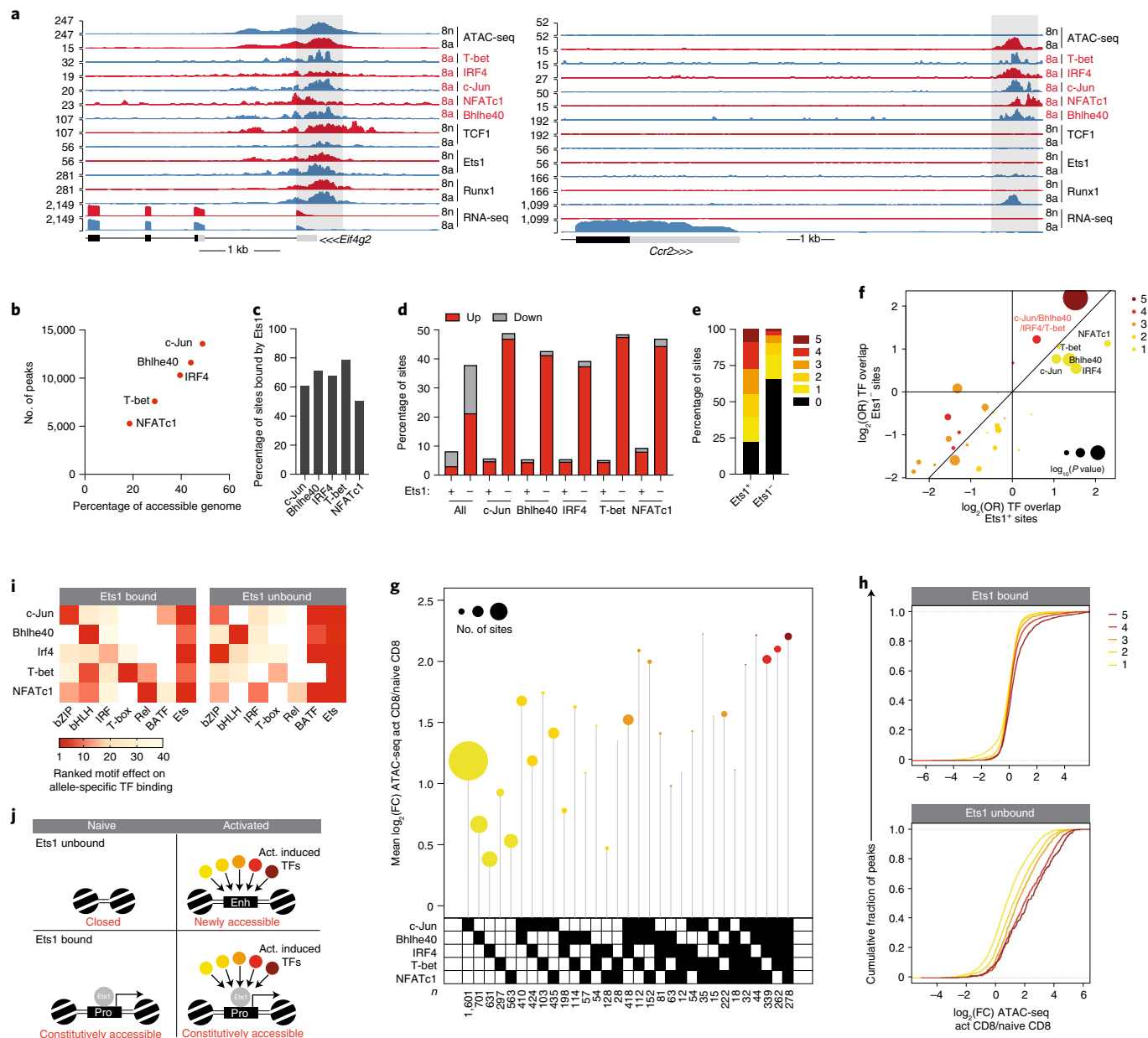


Fig. 3 | Pre-accessible Ets1-bound chromatin regions are not responsive to activation-induced TFs. **a**, Gene tracks of RNA-seq, ATAC-seq and CUT&RUN read coverage at the *Eif4g2* and *Ccr2* loci in naïve and activated CD8 T cells. **b**, Binding of c-Jun, Bhlhe40, IRF4, T-bet and NFATc1 in activated CD8 T cells determined by CUT&RUN. The number of ATAC-seq peaks bound by each TF is shown, together with the fraction of all accessible peaks (>100 ATAC-seq reads in activated T cells) that is bound by each factor. **c**, Fraction of TF-bound ATAC-seq peaks co-bound by Ets1. **d**, Fraction of sites bound by the indicated combination of TFs with more than fourfold higher (up) or lower (down) chromatin accessibility in activated versus naïve CD8 T cells. **e**, Fraction of Ets1-bound and -unbound ATAC-seq peaks bound by 0–5 activation-induced TFs. **f**, Enrichment of TF co-localization at Ets1-bound and -unbound sites occupied by at least one activation-induced TF in activated CD8 T cells. The *P* values were calculated from one-sided Fisher's exact test, followed by the Benjamini-Hochberg procedure. OR, odds ratio. **g**, Fold-change (FC) in chromatin accessibility in activated versus naïve CD8 T cells at Ets1-unbound ATAC-seq peaks occupied by distinct combinations of activation-induced TFs. The data points are scaled according to the number of peaks in each set. **h**, Fold-change in chromatin accessibility in activated versus naïve CD8 T cells at Ets1-bound and -unbound ATAC-seq peaks occupied by 1–5 activation-induced TFs. **i**, Effect of TF-binding motif variation on allelic bias in TF occupancy at Ets1-bound versus -unbound ATAC-seq peaks. Each CUT&RUN experiment is shown on the y axis. The x axis shows the most statistically significant motif for each family. **j**, Model of TF binding and chromatin accessibility changes at Ets1-bound and -unbound regulatory elements. Act. induced, activation-induced.

ous ‘amplifiers’ that can synergize with other activation-dependent TFs (Fig. 5h).

Context-dependent role of TCF1 during T cell activation. In contrast to Runx1 binding to sites either gaining or losing accessibility upon T cell activation, we found that TCF1 bound preferentially to

sites that lost accessibility (Fig. 5c). TCF1-bound sites that did not overlap with Ets1 became less accessible upon T cell activation, consistent with the downregulation of TCF1 and the related TF Lef1 (Fig. 6a and Extended Data Figs. 1f and 5a). Thus, loss of chromatin accessibility upon T cell activation may, to a substantial degree, be explained by downregulation of TCF1 and Lef1, the motifs of which

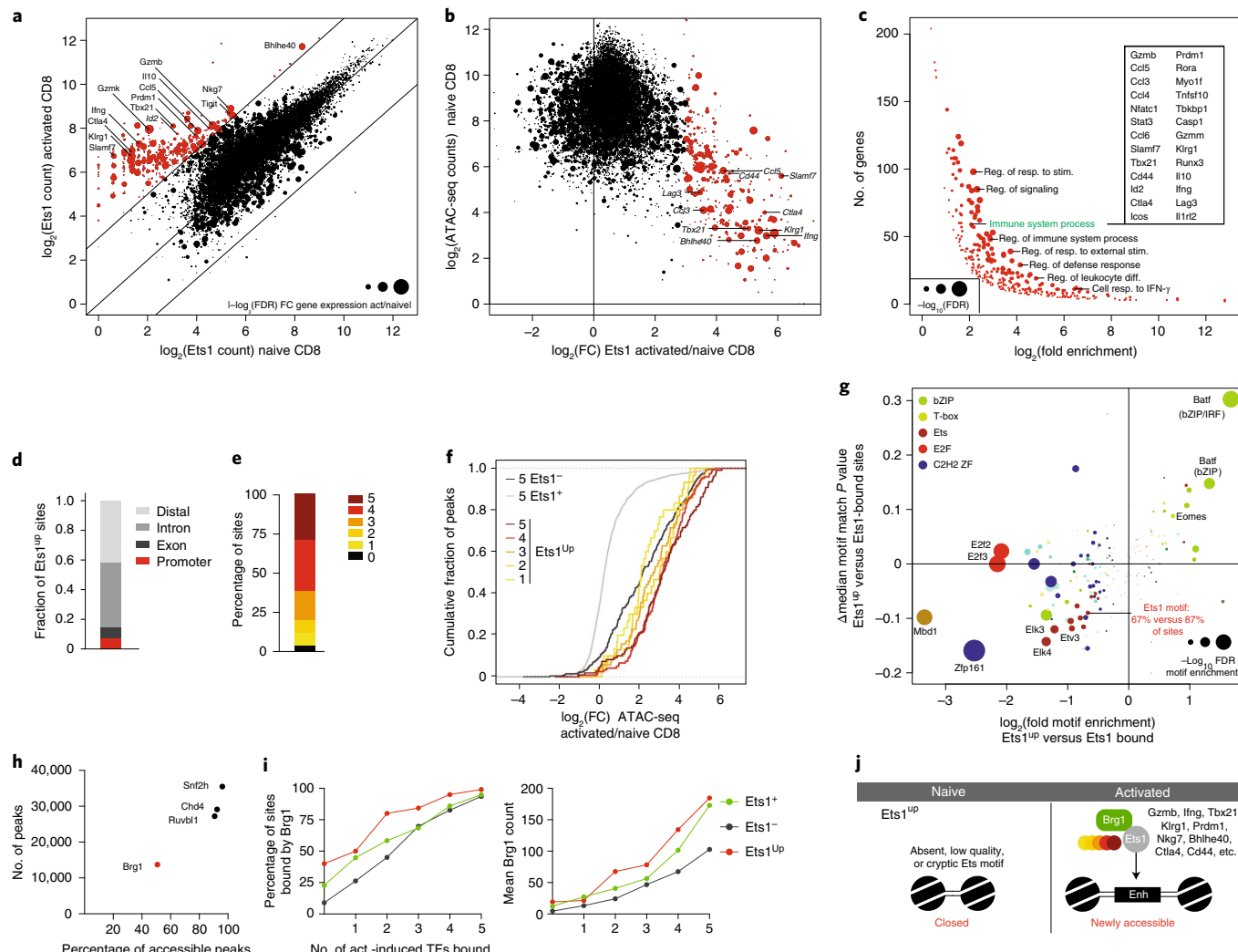


Fig. 4 | A small subset of immune response-related elements recruits Ets1 upon T cell activation. **a**, Ets1 CUT&RUN counts at ATAC-seq peak regions in naive and activated CD8 T cells. The data points are scaled according to the absolute $\log_2(\text{fold-change})$ in expression of the nearest gene in activated versus naive CD8 T cells. A subset of peaks with a more than eightfold increase in Ets1 binding in activated versus naive CD8 T cells (Ets1^{up} sites) is highlighted in red. **b**, Chromatin accessibility in naive CD8 T cells plotted against the $\log_2(\text{fold-change})$ in Ets1 binding in activated versus naive CD8 T cells. Ets1^{up} sites are highlighted in red. **c**, GO term enrichment analysis for genes nearest to ATAC-seq peaks gaining Ets1 binding upon T cell activation (red dots in **a** and **b**). diff., differentiation; FDR, false discovery rate; IFN, interferon; Reg., Regulation; resp., response; stim., stimulus. **d**, The *cis*-regulatory element composition of Ets1^{up} sites. **e**, Fraction of Ets1^{up} sites bound by 0–5 activation-induced TFs. **f**, Changes in chromatin accessibility in activated versus naive CD8 T cells at Ets1^{up} sites bound by 5 activation-induced TFs. Ets1-bound (Ets1⁺) and -unbound (Ets1⁻) elements co-occupied by five activation-induced TFs are shown as a reference. **g**, TF-binding motif enrichment and difference in median (ΔMedian) motif match *P* value at Ets1^{up} versus Ets1-bound ATAC-seq peaks. **h**, Snf2h, Chd4, Ruvbl1 and Brg1 binding measured by CUT&RUN in activated CD8 T cells. The number of ATAC-seq peaks bound by each TF is shown, together with the fraction of all accessible peaks (>100 ATAC-seq reads in activated T cells) that is bound by each factor. **i**, Fraction of Ets1-bound (Ets1⁺), Ets1-unbound (Ets1⁻) and Ets1^{up} peaks co-bound by 0–5 activation-induced TFs that are bound by Brg1 in activated CD8 T cells (left). Mean Brg1 counts at the corresponding peak sets (right). **j**, Model of TF activity at Ets1^{up} elements.

show a positive association with chromatin accessibility in naive T cells (Fig. 1b).

Importantly, activation-induced downregulation of TCF1 was much more pronounced in CD8 than in CD4 T cells, consistent with a stronger reduction in chromatin accessibility in the former (Extended Data Fig. 1f and Fig. 6a). Accordingly, we observed a loss of TCF1-binding intensity by CUT&RUN in activated versus naive CD8 T cells affecting nearly all TCF1 targets (Fig. 6b). Although activation-induced changes in TCF1 binding were associated with corresponding changes in accessibility, we found that many sites that lost TCF1 binding by as much as fourfold in activated versus naive CD8 T cells still maintained or even increased their accessibility (Fig. 6b and Extended Data Fig. 5b). This observation suggested that

loss of TCF1 might be compensated for by the recruitment of other activating TFs. Consistent with this notion, the TCF1 occupied sites that did not recruit activation-induced TFs strongly lost chromatin accessibility upon T cell activation, whereas those recruiting more activation-induced TFs maintained or gained accessibility (Fig. 6c). Thus, in naive CD8 T cells TCF1 may frequently act as a placeholder for activation-induced TFs. Furthermore, we observed that sites at which TCF1 was displaced by multiple activation-induced TFs were similarly accessible in activated CD4 versus CD8 T cells, despite the selective maintenance of TCF1 levels in the former, suggesting that TCF1 became dispensable for the maintenance of chromatin accessibility at these sites after T cell activation (Fig. 6c). Conversely, sites at which TCF1 was not displaced by one or more activation-induced

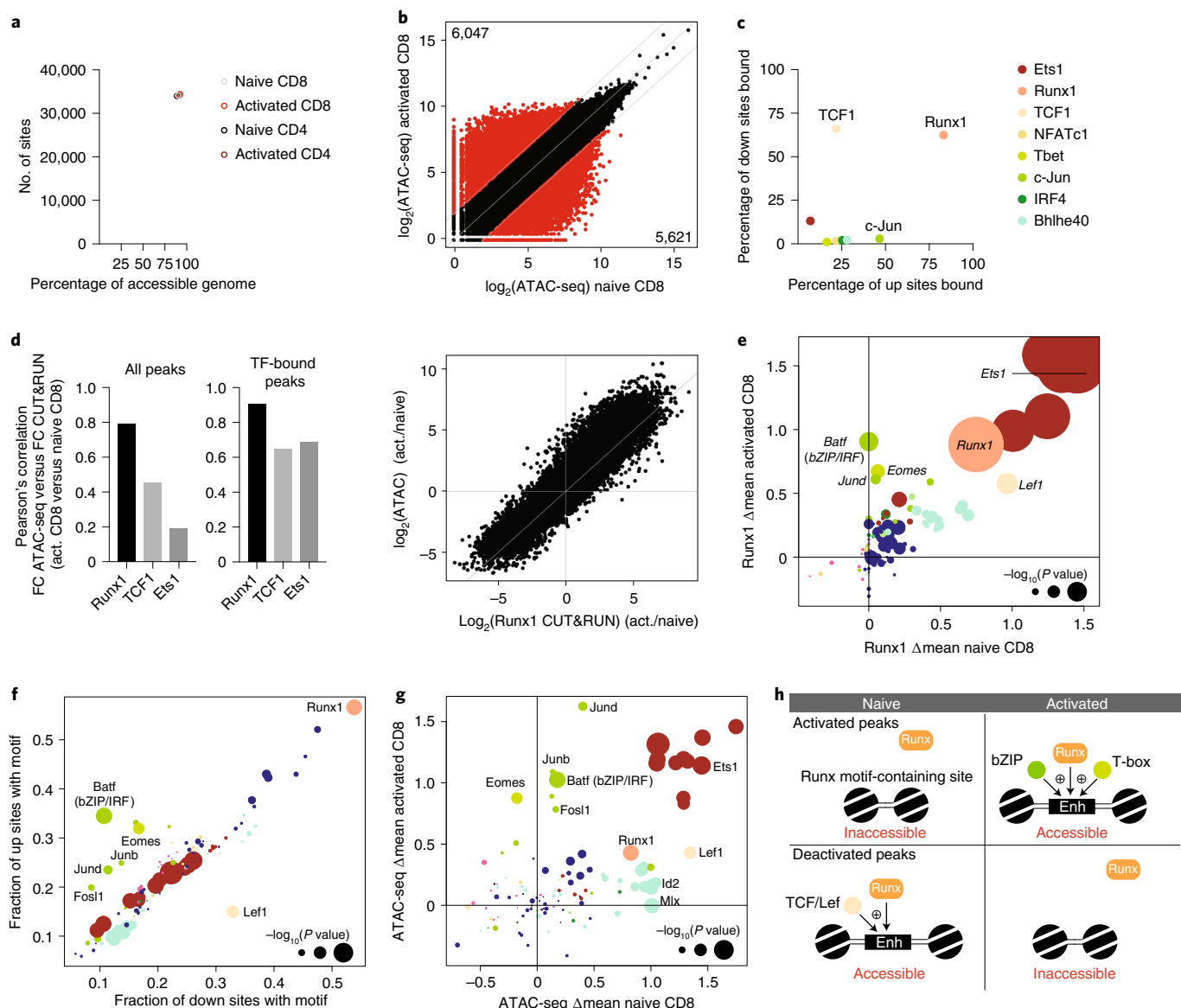


Fig. 5 | Activation-dependent TF partners influence Runx1 localization. **a**, Runx1 binding was determined in naive and activated CD4 and CD8 T cells using CUT&RUN. The number of ATAC-seq peaks bound by Runx1 is shown, together with the fraction of all accessible peaks (>100 ATAC-seq reads) that is bound by Runx1. **b**, Chromatin accessibility in naive and activated CD8 T cells across all ATAC-seq atlas peaks. Peaks with more than fourfold differential accessibility are highlighted in red. The number of peaks with higher and lower chromatin accessibility in naive and activated CD8 T cells is indicated. **c**, Fraction of differentially accessible chromatin regions (highlighted in **b**) bound by each TF. **d**, Pearson's correlation between changes in chromatin accessibility and changes in TF-binding intensity for Runx1, TCF1 and Ets1 in activated versus naive CD8 T cells. Analysis was done for all peaks or only the peaks bound by the respective TF. A scatter plot shows the fold-change in Runx1 binding and the fold-change in chromatin accessibility in activated versus naive CD8 T cells. **e**, Effect of TF-binding motif variation on Runx1 binding in naive and activated CD8 T cells. Only the peaks that were differentially accessible in naive and activated CD8 T cells (**b**) were included in the analysis. The data points are colored by TF family and scaled according to the $-\log_{10}(P \text{ value})$ of a two-sided Student's *t*-test comparing allelic ratios between peaks with stronger motif matches on the B6 versus the Cast allele. The most significant *P* value obtained across the two cell types (naive and activated CD8) was used for scaling. **f**, TF-binding motif occurrence at peaks gaining (up sites) or losing (down sites) accessibility upon T cell activation. The motif significance of global allelic imbalance was calculated using a two-sided Student's *t*-test with the same approach as in Fig. 1e. **g**, Effect of TF-binding motif variation on chromatin accessibility in naive and activated CD8 T cells. A two-sided Student's *t*-test was used to calculate motif *P* values as described in Fig. 1e. Only peaks that were differentially accessible in naive and activated CD8 T cells (**b**) were included in the analysis. **h**, Model of Runx1 activity at sites gaining or losing chromatin accessibility upon T cell activation.

TFs became differentially accessible in activated CD4 and CD8 T cells, in accordance with varying amounts of TCF1 in these cells (Fig. 6c).

Our analysis also revealed a small subset of sites (794 sites or ~3% of all TCF1 targets) that acquired TCF1 binding only upon T cell activation (Fig. 6b and Extended Data Fig. 5c). These sites

were largely identical in CD4 and CD8 T cells, although they were less strongly bound in the latter. Thus, despite a global reduction in TCF1-binding intensity in activated CD8 T cells, a small subset of sites still recruited TCF1 upon T cell activation. The vast majority of these TCF1^{up} peaks were not bound by Ets1 but overlapped substantially with sites combinatorially bound by activation-induced TFs

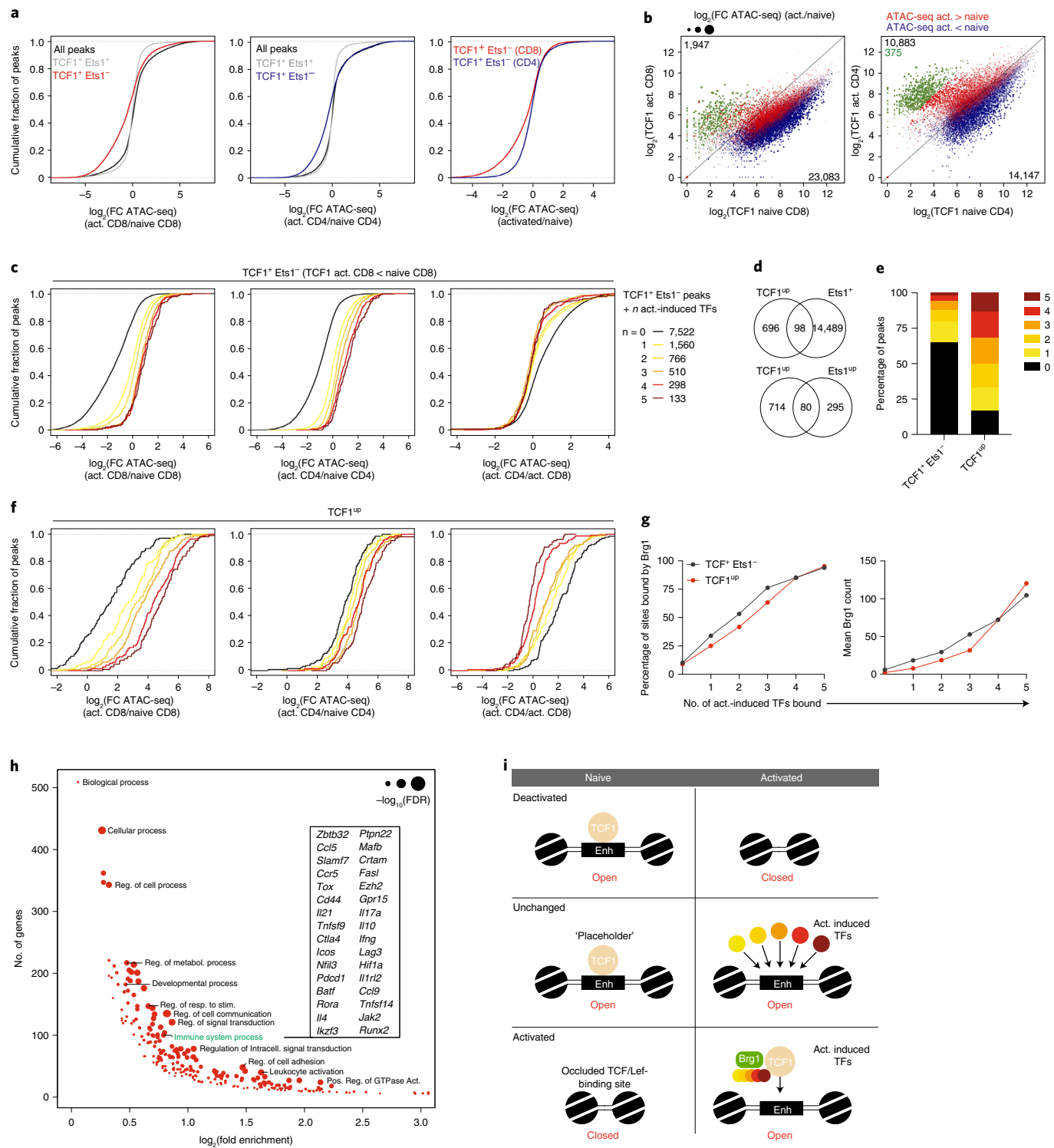


Fig. 6 | Context-dependent functions of TCF1 in naive and activated CD4 and CD8 T cells. **a**, Chromatin accessibility changes between naive and activated CD4 and CD8 T cells at ATAC-seq peaks bound by TCF1 with or without Ets1. All peaks denote peaks with >100 reads in one or more cell types. **b**, TCF1 CUT&RUN signal at ATAC-seq peak regions in naive and activated CD4 and CD8 T cells. The data points are scaled according to the fold-change in chromatin accessibility, and colored blue or red according to the directionality of the accessibility change. A subset of peaks that has strong preferential binding of TCF1 in activated T cells was identified in CD4 T cells and highlighted in green. **c**, Chromatin accessibility changes between naive and activated CD4 and CD8 T cells at Ets1⁺TCF1⁻ ATAC-seq peaks bound by 0–5 activation-induced TFs. Analysis was restricted to peaks with lower TCF1 binding in activated versus naive CD8 T cells. **d**, Overlap between TCF1^{up} peaks (green peaks in **b**) and Ets1-bound ATAC-seq peaks (top) or TCF1^{up} peaks (bottom). **e**, Fraction of TCF1+Ets1- peaks and TCF1^{up} peaks bound by 0–5 activation-induced TFs. **f**, Chromatin accessibility changes in naive and activated CD4 and CD8 T cells at TCF1^{up} peaks bound by 0–5 activation-induced TFs. **g**, Fraction of TCF1+Ets1- peaks and TCF1^{up} peaks co-bound by 0–5 activation-induced TFs that are bound by Brg1 in activated CD8 T cells (left). Mean Brg1 count at the corresponding peak sets (right) is shown. **h**, GO term enrichment analysis for genes nearest to TCF1^{up} peaks (green dots in **b**). **i**, Model of TF activity at TCF1-bound regulatory elements. See the legend for Fig. 4 for abbreviations.

(Fig. 6d,e). TCF1^{up} sites strongly gained accessibility upon T cell activation, particularly when bound by multiple activation-induced TFs (Fig. 6f). Depending on the number of activation-induced TFs that was bound, TCF1^{up} sites responded differentially to activation in CD4 versus CD8 T cells. Specifically, when fewer activation-induced TFs were recruited, chromatin remodeling occurred in a CD4 T cell-specific manner. This observation further supports the notion that activation-induced TFs may compensate for the loss of TCF1 at a subset of targets after T cell activation.

The observation that, despite high TCF1 expression, TCF1^{up} sites were not bound in naive T cells suggested that TCF1 alone was not sufficient to render these sites accessible. Thus, despite the previously described role of TCF1 as a pioneer factor capable of binding to inaccessible repressed chromatin regions, its activity was not sufficient to induce accessibility at a subset of its potential binding sites. Analysis of TCF1^{up} sites revealed that most of these regions contained intact and high-quality TCF1/Lef1 motifs, but were relatively depleted of Ets, zinc-finger and bHLH motifs, the last of which had a positive effect on chromatin accessibility selectively in naive T cells (Extended Data Figs. 5d,e and 1b). Conversely, bZIP motifs were strongly enriched at TCF1^{up} sites and, accordingly, we found that most of these sites were bound by c-Jun (Extended Data Fig. 5f). Finally, we observed that sites bound by TCF1 in the absence of activation-induced TFs were rarely occupied by Brg1, the recruitment of which was associated with the binding of activation-induced TFs (Fig. 6g). Together, these observations suggest that, at a subset of targets, TCF1 cannot bind to its cognate motif in an autonomous manner but requires assistance from activation-induced TFs. Interestingly, we found that, similar to Ets1^{up} sites, TCF1^{up} sites were associated with immune response-related genes, as well as genes involved in signal transduction, cell adhesion and cellular communication (Fig. 6h). Thus, regulatory elements associated with some of the most strongly induced and well-characterized immune response genes showed rather atypical patterns of Ets1 and TCF1 recruitment which were not representative of the prevalent function of these TFs. Although TCF1 typically acted as a naive T cell-specific activator, our results suggest that it plays additional, previously unappreciated roles as a placeholder for activation-induced TFs and as an activation-dependent cofactor (Fig. 6i).

Graded activity of chromatin-modifying TFs in T cell subsets. To assess the generalizability of our observations across distinct T cell subsets, we performed single-cell (sc)ATAC-seq analysis on total splenic CD4 and CD8 T cells from LCMV-infected (B6/Cast) F1 animals on day 7 post-infection. This analysis revealed several distinct T cell subsets, including naive and memory CD4 and CD8 T cells, regulatory T (T_{reg}) cells, type 1 helper T (T_{H1}) cells, follicular helper T (T_{FH}) cells and a spectrum of effector CD8 T cells (Fig. 7a,b and Extended Data Fig. 6a). To identify regulators of chromatin accessibility across these subsets, we analyzed the effects of TF-binding motif polymorphisms on allele-specific, pseudo-bulk scATAC-seq counts from these populations. Motifs affecting chromatin accessibility across T cell subpopulations were largely similar to those identified in bulk cell analyses (Extended Data Fig. 6b). Consistently, genetic variation in Ets, Runx, IRF and bZIP motifs strongly affected chromatin accessibility in all subsets. A comparison between the two main subpopulations of CD4 T cells arising in response to viral infection, T_{H1} cells and T_{FH} cells, revealed a stronger effect of the T-box motif variation on chromatin accessibility in the former and a stronger effect of Sox motif variants in the latter (Fig. 7c). Accordingly, we found that chromatin regions bound by T-bet were more accessible in T_{H1} cells, whereas regions bound by TCF1 were more accessible in T_{FH} cells. Importantly, this effect was observed only at regions not bound by Ets1 (Fig. 7d). Consistent with our bulk cell analysis, Ets1-bound sites showed very high chromatin accessibility across all T cell subsets, whereas regions bound

by activation-induced TFs in the absence of Ets1 were dynamically regulated (Fig. 7e). Similarly, Ets1^{up} sites and TCF1^{up} sites showed dynamic regulation with much higher accessibility across all activated T cell subsets compared with naive T cells from the same mice (Extended Data Fig. 6c). Together, our observations suggest that the major drivers of chromatin accessibility are similar across T cell subsets responding to acute LCMV infection, with graded activity of Sox and T-box family TFs at sites not bound by Ets1, accounting for many of the differences between T_{H1} and T_{FH} cells.

Discussion

T cell activation induces transcriptional and epigenetic changes that underlie the acquisition of specialized effector functions. In the present study, we leveraged natural genetic variation between laboratory and wild-derived inbred mice to identify the TFs, the DNA-binding motifs of which shape chromatin accessibility and gene expression in naive and activated T cells during acute LCMV infection. Most TF-binding motifs showed a positive effect on chromatin accessibility, with only a few dedicated repressive motifs identified, including nuclear receptor and specific zinc-finger motifs. TF families with those motifs that had either no or only a limited effect included E2F, Forkhead, Gata, STAT and Smad. Some TFs belonging to these families probably carry out relatively specialized functions affecting only minor subsets of the loci to which they bind or acting transiently shortly after acute stimulation.

Considering the many TFs expressed in T cells, our studies unexpectedly identified just a few ‘heavy lifters’ with binding motifs that most strongly affected chromatin accessibility. Three representative TFs belonging to these families, Ets1, Runx1 and TCF1, together occupied ~94% of all accessible chromatin regions in naive T cells. Ets1 binding defined peaks enriched at promoters of housekeeping genes with accessibility that remained largely unchanged upon T cell activation. Interestingly, most of the binding sites for activation-induced TFs overlapped with Ets1-bound peaks, suggesting that these factors affect chromatin accessibility only at a small fraction of the regions that they occupy.

In addition to constitutively bound sites, a subset of elements acquired Ets1 binding anew upon T cell activation and were preferentially associated with immune response genes. Although the exact mechanisms underlying the new recruitment of Ets1 remain unknown, we postulate that, in addition to the presence of weaker Ets motifs, barriers to Ets1 binding may include tightly packed chromatin associated with repressive histone modifications and DNA methylation. In accordance with this model, it was reported that methylation of an intronic regulatory element in the *Foxp3* locus could prevent the binding and activity of Ets1 at its consensus motifs¹⁸. In addition, both activation-dependent and -independent partners, including Runx1 and bZIP/AP1 family TFs, could stabilize Ets1 binding at distinct sets of regulatory elements^{19–22}. Finally, phosphorylation of Ets1 at multiple residues can destabilize DNA binding or promote cofactor recruitment, suggesting additional mechanisms that could drive activation-state, specific-binding site selection^{23–26}.

T cells express multiple Ets family TFs that play nonredundant roles in their development or activation^{27–33}. Although all family members share a highly conserved Ets domain and recognize a consensus motif, their binding sites *in vivo* may be either shared or member specific^{34–36}. A comparison of binding sites for three Ets family TFs in a human T cell line revealed that redundant binding of multiple factors was common and enriched at transcription start sites of housekeeping genes, whereas nonredundant binding was rare and enriched at cell type-specific enhancers^{37,38}. Based on these observations, we speculate that most constitutively bound Ets1 targets identified in our study are co-occupied by multiple Ets family TFs, whereas Ets1^{up} sites may be bound specifically by Ets1. Importantly, genetic variation in Ets motifs also affected chromatin

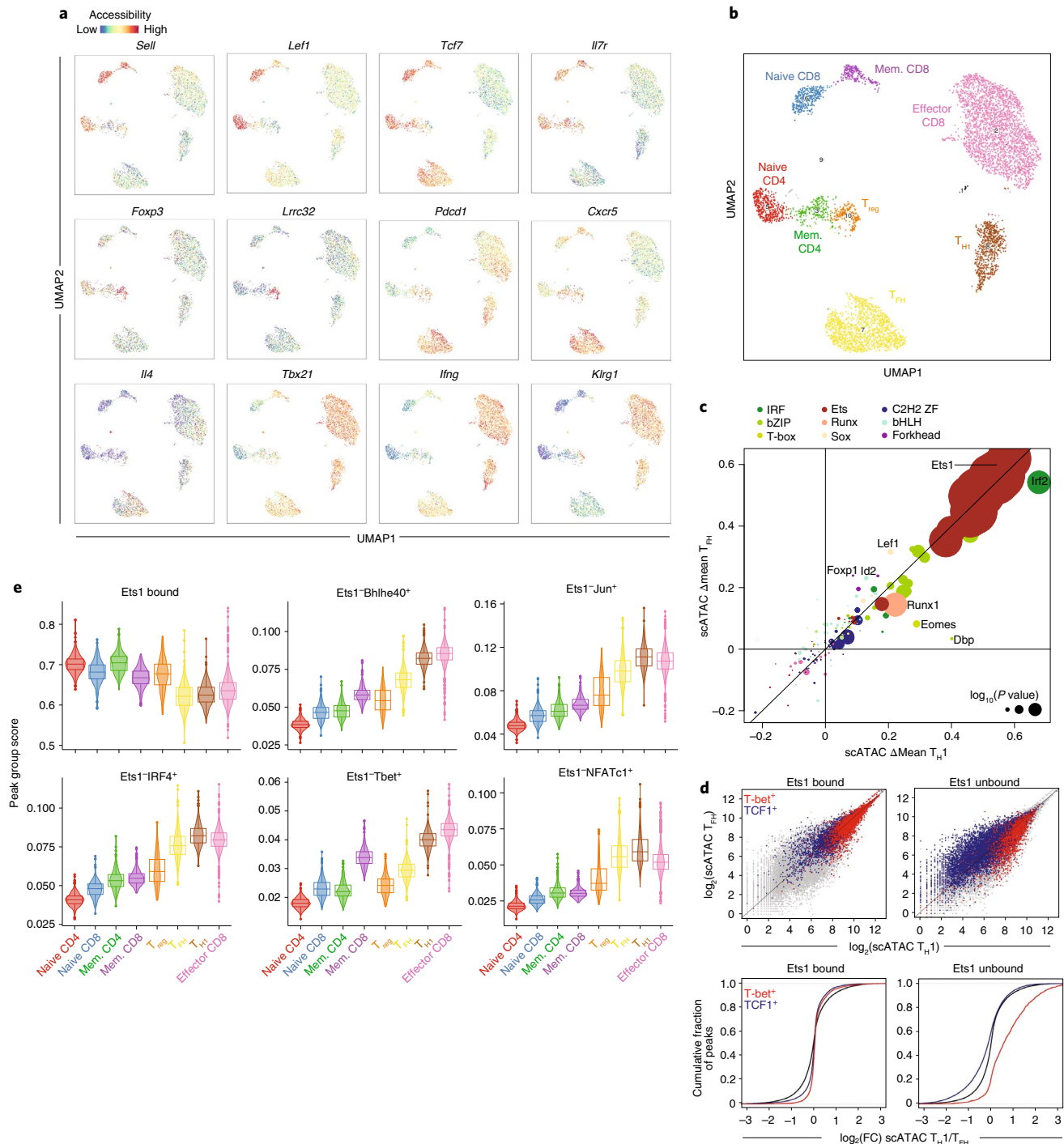


Fig. 7 | Drivers of chromatin accessibility across T cell subpopulations. **a**, Chromatin accessibility at selected loci across T cell subpopulations in LCMV-infected (B6/Cast) F1 mice measured by scATAC-seq on total splenic CD4 and CD8 T cells ($n=6,043$ cells). **b**, Subset annotation. Mem., memory. **c**, Effect of genetic variation in TF-binding motifs on allele-specific, pseudo-bulk scATAC-seq counts in T_{H1} and T_{FH} cells. Data points are colored by TF family and scaled according to the $-\log_{10}(P \text{ value})$ of a two-sided Student's *t*-test comparing the allelic ratios between peaks with stronger matches on the B6 versus the Cast allele. **d**, Pseudo-bulk scATAC-seq data showing accessibility in T_{H1} versus T_{FH} cells at Ets1-bound or -unbound sites co-occupied by T-bet or TCF1. Gray dots (top) and black lines (bottom) show all accessible peaks. **e**, Violin plots and box plots showing accessibility of indicated peak groups across T cell subsets ($n=6,043$ cells). The center line in the box plots represents the median, the box limits represent the 25th and 75th percentiles, and the whiskers are the minimum/maximum values within 1.5 \times the interquartile range ($n=\text{the number of cells in each cell annotation}$ (420 naive CD4; 344 naive CD8; 234 memory CD4; 231 memory CD8; 198 T_{reg}; 1,321 T_{FH}; 652 T_{H1}; 2,583 effector CD8)).

accessibility and TF binding at sites not occupied by Ets1, suggesting that other family members may bind to these elements. Together, our results suggest that Ets family TFs play a uniquely dominant role in shaping the transcriptome and epigenome of T cells.

In contrast to Ets1, many Runx1-binding sites were activation state dependent. Runx motifs were present at most differentially accessible ATAC-seq peaks and affected allele-specific chromatin accessibility. Thus, Runx family TFs may act as universal amplifiers

of gene-regulatory activity. Consistent with this model, Runx TFs have been reported to interact with a large variety of TFs, including Ets1, TCF1, Lef1, Gata3, Bcl11b, T-bet, Rorγt, Foxp1 and Foxp3 (refs. [20,39–43](#)). Interactions with some of these TFs can enhance or stabilize Runx1 binding and transactivation potential^{[19,39](#)}. In addition to Runx1, T cells also express Runx2 and Runx3, which may bind dynamically to cell state-specific regulatory elements to carry out partially redundant functions during T cell development and activation^{[44](#)}. A nonredundant role for Runx3 in CD8 lineage specification has been extensively characterized and could potentially be mediated by its association with a unique set of cofactors^{[40,45,46](#)}. Although our study suggests that intact Runx motifs have a net positive effect on chromatin accessibility in mature T cells, Runx TFs have also been shown to engage in gene repression and associate with co-repressors, including TLE (transducin-like enhancer of split) and G9a^{[40,47,48](#)}. Therefore, the division of labor between individual Runx family TFs and their roles as activators versus repressors remain to be fully elucidated.

We found that TCF1-bound sites typically lost chromatin accessibility upon T cell activation. These changes occurred selectively at sites not co-occupied by Ets1 or activation-induced TFs and were more pronounced in CD8 versus CD4 T cells, consistent with lower levels of TCF1 in the former. Together with the positive effect of intact TCF/Lef motifs on chromatin accessibility, these observations are consistent with the notion that TCF1 acts primarily as an activator^{[49](#)}. Interestingly, we identified a substantial fraction of sites at which TCF1 was displaced by activation-induced TFs. Despite the loss of TCF1, these elements maintained their accessibility upon T cell activation. It is tempting to speculate that this placeholder activity of TCF1 may underlie its function in maintaining differentiation potential or ‘stem-ness’. Finally, we also identified a subset of TCF1 targets that was selectively bound only in activated T cells and frequently co-occupied by activation-induced TFs. It remains unclear what prevents TCF1 from binding to its activation-dependent sites in naive T cells. Although TCF1 is capable of binding and remodeling closed chromatin regions marked by repressive histone modifications, this capacity alone was apparently not sufficient to drive accessibility at these sites^{[49](#)}.

Our findings offer a new perspective on the interplay between the activities of critical TFs that define T cell identity and improve our understanding of transcriptional and epigenetic regulation in resting and activated CD4 and CD8 T cells.

Online content

Any methods, additional references, Nature Research reporting summaries, extended data, supplementary information, acknowledgements, peer review information; details of author contributions and competing interests; and statements of data and code availability are available at <https://doi.org/10.1038/s41590-021-01086-x>.

Received: 19 February 2021; Accepted: 2 November 2021;

Published online: 22 December 2021

References

- Kaech, S. M. & Cui, W. Transcriptional control of effector and memory CD8⁺ T cell differentiation. *Nat. Rev. Immunol.* **12**, 749–761 (2012).
- Zhu, J., Yamane, H. & Paul, W. E. Differentiation of effector CD4 T cell populations (*). *Annu. Rev. Immunol.* **28**, 445–489 (2010).
- McLane, L. M., Abdel-Hakeem, M. S. & Wherry, E. J. CD8 T cell exhaustion during chronic viral infection and cancer. *Annu. Rev. Immunol.* **37**, 457–495 (2019).
- Mackay, L. K. & Kallies, A. Transcriptional regulation of tissue-resident lymphocytes. *Trends Immunol.* **38**, 94–103 (2017).
- Milner, J. J. & Goldrath, A. W. Transcriptional programming of tissue-resident memory CD8. *Curr. Opin. Immunol.* **51**, 162–CD169 (2018).
- Vaquerizas, J. M., Kummerfeld, S. K., Teichmann, S. A. & Luscombe, N. M. A census of human transcription factors: function, expression and evolution. *Nat. Rev. Genet.* **10**, 252–263 (2009).
- Gray, P. A. et al. Mouse brain organization revealed through direct genome-scale TF expression analysis. *Science* **306**, 2255–2257 (2004).
- Badis, G. et al. Diversity and complexity in DNA recognition by transcription factors. *Science* **324**, 1720–1723 (2009).
- Jolma, A. et al. DNA-binding specificities of human transcription factors. *Cell* **152**, 327–339 (2013).
- Gerstein, M. B. et al. Architecture of the human regulatory network derived from ENCODE data. *Nature* **489**, 91–100 (2012).
- Lee, T. I. & Young, R. A. Transcriptional regulation and its misregulation in disease. *Cell* **152**, 1237–1251 (2013).
- Spitz, F. & Furlong, E. E. Transcription factors: from enhancer binding to developmental control. *Nat. Rev. Genet.* **13**, 613–626 (2012).
- Chang, J. T., Wherry, E. J. & Goldrath, A. W. Molecular regulation of effector and memory T cell differentiation. *Nat. Immunol.* **15**, 1104–1115 (2014).
- Hosokawa, H. & Rothenberg, E. V. How transcription factors drive choice of the T cell fate. *Nat. Rev. Immunol.* <https://doi.org/10.1038/s41577-020-00426-6> (2020).
- van der Veeken, J. et al. The transcription factor Foxp3 shapes regulatory T cell identity by tuning the activity of *trans*-acting intermediaries. *Immunity* **53**, 971–984.e975 (2020).
- van der Veeken, J. et al. Natural genetic variation reveals key features of epigenetic and transcriptional memory in virus-specific CD8 T cells. *Immunity* **50**, 1202–1217.e1207 (2019).
- Hota, S. K. & Bruneau, B. G. ATP-dependent chromatin remodeling during mammalian development. *Development* **143**, 2882–2897 (2016).
- Polansky, J. K. et al. Methylation matters: binding of Ets-1 to the demethylated Foxp3 gene contributes to the stabilization of Foxp3 expression in regulatory T cells. *J. Mol. Med.* **88**, 1029–1040 (2010).
- Wotton, D., Ghysdael, J., Wang, S., Speck, N. A. & Owen, M. J. Cooperative binding of Ets-1 and core binding factor to DNA. *Mol. Cell Biol.* **14**, 840–850 (1994).
- Kim, W. Y. et al. Mutual activation of Ets-1 and AML1 DNA binding by direct interaction of their autoinhibitory domains. *EMBO J.* **18**, 1609–1620 (1999).
- Wang, C. Y. et al. Activation of the granulocyte–macrophage colony-stimulating factor promoter in T cells requires cooperative binding of Elf-1 and AP-1 transcription factors. *Mol. Cell Biol.* **14**, 1153–1159 (1994).
- Bassuk, A. G. & Leiden, J. M. A direct physical association between ETS and AP-1 transcription factors in normal human T cells. *Immunity* **3**, 223–237 (1995).
- Pognonc, P., Boulukos, K. E., Gesquière, J. C., Stéhelin, D. & Ghysdael, J. Mitogenic stimulation of thymocytes results in the calcium-dependent phosphorylation of c-ets-1 proteins. *EMBO J.* **7**, 977–983 (1988).
- Rabaut, B. & Ghysdael, J. Calcium-induced phosphorylation of ETS1 inhibits its specific DNA binding activity. *J. Biol. Chem.* **269**, 28143–28151 (1994).
- Cowley, D. O. & Graves, B. J. Phosphorylation represses Ets-1 DNA binding by reinforcing autoinhibition. *Genes Dev.* **14**, 366–376 (2000).
- Foulds, C. E., Nelson, M. L., Blaszcak, A. G. & Graves, B. J. Ras/mitogen-activated protein kinase signaling activates Ets-1 and Ets-2 by CBP/p300 recruitment. *Mol. Cell Biol.* **24**, 10954–10964 (2004).
- Bories, J. C. et al. Increased T-cell apoptosis and terminal B-cell differentiation induced by inactivation of the Ets-1 proto-oncogene. *Nature* **377**, 635–638 (1995).
- Muthusamy, N., Barton, K. & Leiden, J. M. Defective activation and survival of T cells lacking the Ets-1 transcription factor. *Nature* **377**, 639–642 (1995).
- Mélet, F., Motro, B., Rossi, D. J., Zhang, L. & Bernstein, A. Generation of a novel Fli-1 protein by gene targeting leads to a defect in thymus development and a delay in Friend virus-induced erythroleukemia. *Mol. Cell Biol.* **16**, 2708–2718 (1996).
- Kim, C. J. et al. The transcription factor Ets1 suppresses T follicular helper type 2 cell differentiation to halt the onset of systemic lupus erythematosus. *Immunity* **49**, 1034–1048.e1038 (2018).
- Anderson, M. K., Hernandez-Hoyos, G., Diamond, R. A. & Rothenberg, E. V. Precise developmental regulation of Ets family transcription factors during specification and commitment to the T cell lineage. *Development* **126**, 3131–3148 (1999).
- Yamada, T., Park, C. S., Mamontkin, M. & Lacorazza, H. D. Transcription factor ELF4 controls the proliferation and homing of CD8⁺ T cells via the Krüppel-like factors KLF4 and KLF2. *Nat. Immunol.* **10**, 618–626 (2009).
- Luo, C. T. et al. Ets transcription factor GABP controls T cell homeostasis and immunity. *Nat. Commun.* **8**, 1062 (2017).
- Hollenhorst, P. C., McIntosh, L. P. & Graves, B. J. Genomic and biochemical insights into the specificity of ETS transcription factors. *Annu. Rev. Biochem.* **80**, 437–471 (2011).
- Thompson, C. B. et al. *cis*-acting sequences required for inducible interleukin-2 enhancer function bind a novel Ets-related protein, Elf-1. *Mol. Cell Biol.* **12**, 1043–1053 (1992).
- Wang, C. Y., Petryniak, B., Ho, I. C., Thompson, C. B. & Leiden, J. M. Evolutionarily conserved Ets family members display distinct DNA binding specificities. *J. Exp. Med.* **175**, 1391–1399 (1992).

37. Hollenhorst, P. C., Shah, A. A., Hopkins, C. & Graves, B. J. Genome-wide analyses reveal properties of redundant and specific promoter occupancy within the ETS gene family. *Genes Dev.* **21**, 1882–1894 (2007).
38. Hollenhorst, P. C. et al. DNA specificity determinants associate with distinct transcription factor functions. *PLoS Genet.* **5**, e1000778 (2009).
39. Giese, K., Kingsley, C., Kirshner, J. R. & Grosschedl, R. Assembly and function of a TCR alpha enhancer complex is dependent on LEF-1-induced DNA bending and multiple protein–protein interactions. *Genes Dev.* **9**, 995–1008 (1995).
40. Verbaro, D. J., Sakurai, N., Kim, B., Shinkai, Y. & Egawa, T. Cutting edge: the histone methyltransferase G9a is required for silencing of helper T lineage-associated genes in proliferating CD8 T cells. *J. Immunol.* **200**, 3891–3896 (2018).
41. Lazarevic, V. et al. T-bet represses T_H17 differentiation by preventing Runx1-mediated activation of the gene encoding ROR γ t. *Nat. Immunol.* **12**, 96–104 (2011).
42. Zhang, F., Meng, G. & Strober, W. Interactions among the transcription factors Runx1, ROR γ mat and Foxp3 regulate the differentiation of interleukin 17-producing T cells. *Nat. Immunol.* **9**, 1297–1306 (2008).
43. Zheng, Y. et al. Role of conserved non-coding DNA elements in the Foxp3 gene in regulatory T-cell fate. *Nature* **463**, 808–812 (2010).
44. Shin, B. et al. Runx1 and Runx3 drive progenitor to T-lineage transcriptome conversion in mouse T cell commitment via dynamic genomic site switching. *Proc. Natl Acad. Sci. USA* <https://doi.org/10.1073/pnas.2019655118> (2021)
45. Taniuchi, I. et al. Differential requirements for Runx proteins in CD4⁺ repression and epigenetic silencing during T lymphocyte development. *Cell* **111**, 621–633 (2002).
46. Egawa, T., Tillman, R. E., Naoe, Y., Taniuchi, I. & Littman, D. R. The role of the Runx transcription factors in thymocyte differentiation and in homeostasis of naive T cells. *J. Exp. Med.* **204**, 1945–1957 (2007).
47. Levanon, D. et al. Transcriptional repression by AML1 and LEF-1 is mediated by the TLE/Groucho corepressors. *Proc. Natl Acad. Sci. USA* **95**, 11590–11595 (1998).
48. Setoguchi, R. et al. Repression of the transcription factor Th-POK by Runx complexes in cytotoxic T cell development. *Science* **319**, 822–825 (2008).
49. Johnson, J. L. et al. Lineage-determining transcription factor TCF-1 initiates the epigenetic identity of T cells. *Immunity* **48**, 243–257.e210 (2018).

Publisher's note Springer Nature remains neutral with regard to jurisdictional claims in published maps and institutional affiliations.

© The Author(s), under exclusive licence to Springer Nature America, Inc. 2021

Methods

Mice. Animals were housed at the Memorial Sloan Kettering Cancer Center (MSKCC) animal facility under specific pathogen-free conditions on a 12-h light:dark cycle under ambient conditions with free access to food and water. All studies were performed under protocol 08-10-023 and approved by the MSKCC Institutional Animal Care and Use Committee. Mice used in the present study had no previous history of experimentation or exposure to drugs. Male Cast/Eij mice were purchased from Jackson Laboratory and bred to female B6 mice to generate F1 offspring. Adult mice (aged >6 weeks) were used for experiments.

LCMV infection. LCMV Armstrong was grown in BHK cells and viral titers were determined using a plaque assay in Vero cells. Mice were infected with 2×10^5 plaque-forming units (p.f.u.) by intraperitoneal injection.

Antibodies. The following antibodies were used for CUT&RUN: Runx1 (Thermo Fisher Scientific, catalog no. PA5-19638), TCF1 (Cell Signaling Technology, catalog no. 2203S), Ets1 (Cell Signaling Technology, catalog no. 14069), T-bet (Santa Cruz Biotechnology, catalog no. sc-21003 X), IRF4 (Santa Cruz Biotechnology, catalog no. sc-6059), c-Jun (Abcam, catalog no. ab31419), NFATc1 (BioLegend, catalog no. 649607), Blhle40 (Novus Biologicals, catalog no. NB100-1800SS), Brg1 (Abcam, catalog no. ab110641), Chd4 (Abcam, catalog no. ab72418), Ruvbl1 (Proteintech group, catalog no. 10210-2-AP) and Snf2h (Abcam, catalog no. ab3749).

The following clones of fluorescently conjugated antibodies were obtained from BD Biosciences, BioLegend, Thermo Fisher Scientific or Tonbo Bioscience, and used for flow cytometry at a 1:400 dilution: CD45 (30-F11), TCR β (H57-597), CD4 (RM4-5), CD8a (53-6.7), CD44 (IM7) and CD62L (MEL-14).

Cell staining and flow cytometry. Single-cell suspensions of spleens were prepared in ice-cold cell isolation buffer (phosphate-buffered saline (PBS) with 2 mM EDTA and 1% fetal calf serum) and subjected to red blood cell lysis using ACK buffer (150 mM NH₄Cl, 10 mM KHCO₃, 0.1 mM Na₂EDTA, pH 7.3). T cells were enriched using Dynabeads FlowComp mouse CD4 and CD8 kits, according to manufacturer's protocol. Cell surface antigens were stained at 4°C for 15 min using a mixture of fluorophore-conjugated antibodies. Phycoerythrin (PE)-labeled H-2D^b LCMV NP396-404 tetramers were generated by mixing biotinylated monomers (National Institutes of Health (NIH) tetramer core facility) with PE-labeled streptavidin. Class I tetramer staining was carried out for 30 min in ice-cold cell isolation buffer using a 1:200 dilution of tetramer. Staining with PE-labeled I-A^b LCMV GP66-77 tetramers (NIH tetramer core facility) was carried out for 30 min at 37°C in complete RPMI medium using a 1:200 dilution of tetramer. Cells were washed and passed through a 100-μm nylon mesh before sorting on a BD Aria II flow cytometer. Post-sort purity was routinely analyzed and typically higher than 95%. Naive T cell populations were sorted as CD44⁻CD62L⁻ CD4 and CD8 T cells from uninfected mice. Activated cells for CUT&RUN were sorted as bulk CD44⁺ CD4 and CD8 T cells on days 7–8 post-infection. Activated and memory cells for RNA-sequencing (RNA-seq) and ATAC-seq were isolated as tetramer⁺ CD4 and CD8 T cells on day 7 or day 60 post-infection, respectively. Flow cytometry data were acquired using FACS Diva (BD) and analyzed using FlowJo.

RNA-seq library preparation and sequencing. Cell populations were double sorted straight into 1 ml of TRIzol reagent (Thermo Fisher Scientific, catalog no. 15596018). After addition of 200 μl of chloroform, RNA was precipitated from the aqueous phase by the addition of isopropanol and linear acrylamide. RNA was washed with 75% ethanol and resuspended in RNase-free water. After RiboGreen quantification and quality control by Agilent BioAnalyzer, 3.4 ng of total RNA underwent amplification using the SMART-Seq v4 Ultra Low Input RNA Kit (Clontech, catalog no. 63488), with 12 cycles of amplification. Subsequently, 300 ng of amplified complementary DNA was used to prepare libraries with the KAPA Hyper Prep Kit (Kapa Biosystems, catalog no. KK8504) using 8 cycles of PCR. Samples were barcoded and run on a HiSeq 4000 in a PE100 run, using the HiSeq 3000/4000 SBS Kit (Illumina). An average of 32×10^6 paired reads were generated per sample and the percentage of messenger RNA bases per sample ranged from 51% to 73%.

ATAC-seq library preparation and sequencing. ATAC-seq libraries were prepared as described⁵⁰. Cells, 5×10^4 , were washed in ice-cold PBS and lysed using ATAC-seq lysis buffer (10 mM Tris-HCl, pH 7.4, 10 mM NaCl, 3 mM MgCl₂, 0.1% IGEPAL CA-630). After lysis, cells were incubated in 1× transposition buffer (Nextera TD buffer) containing 2.5 μl of Nextera Tn5 transposase for 30 min at 37°C. Transposed DNA fragments were isolated using QIAGEN MinElute Reaction Cleanup kit and amplified using barcoded primers with Illumina adapter sequences. The number of cycles used for library amplification was determined using a quantitative PCR side reaction. Amplified libraries were purified and size selected using Ampure XP beads using consecutive purifications with bead:sample ratios of 0.5 and 1.8. After PicoGreen quantification and quality control by Agilent BioAnalyzer, libraries were pooled equimolar and run on a HiSeq 2500 in Rapid Mode in a PE100 run, using the HiSeq Rapid SBS Kit (Illumina). The loading concentration was 9.8 pM and a 5% spike-in of PhiX was added to the run to

increase diversity and for quality control purposes. The run yielded an average of 24×10^6 reads per sample.

CUT&RUN library preparation and sequencing. CUT&RUN libraries were prepared as described by Skene et al.⁵¹, with modifications¹⁵. All CUT&RUN experiments were performed on freshly sorted cell populations. For NFATc1 CUT&RUN sorted cells were re-stimulated in vitro for 1 h at 37°C in the presence of 50 ng ml⁻¹ of phorbol-12-myristate-13-acetate (Sigma-Aldrich, catalog no. P8139) and 500 ng ml⁻¹ of ionomycin (Sigma-Aldrich, catalog no. I0634) with 1 μg ml⁻¹ of Brefeldin A (Sigma-Aldrich, catalog no. B6542). Cells were collected in a V-bottomed 96-well plate by centrifugation and washed in antibody buffer (buffer 1 (1× permeabilization buffer from eBioscience Foxp3/Transcription Factor Staining Buffer Set diluted in nuclease-free water, 1× EDTA-free protease inhibitors, 0.5 mM spermidine) containing 2 mM EDTA). Cells were incubated with antibodies (1:200 dilution) for 1 h on ice. After two washes in buffer 1, cells were incubated with pA/G-MNase at 1:4,000 dilution in buffer 1 for 1 h at 4°C. Cells were washed twice in buffer 2 (0.05% (w:v) saponin, 1× EDTA-free protease inhibitors, 0.5 mM spermidine in PBS) and resuspended in calcium buffer (buffer 2 containing 2 mM CaCl₂) to activate micrococcal nuclease. After a 30-min incubation on ice, 2× stop solution (20 mM EDTA, 4 mM (ethylenebis(oxonitriolo)) tetra-acetate (EGTA) in buffer 2) was added and cells were incubated for 10 min in a 37°C incubator to release cleaved chromatin fragments. Supernatants were collected by centrifugation and DNA was extracted using a QIAGEN MinElute kit.

CUT&RUN libraries were prepared using the Kapa Hyper Prep Kit (Kapa Biosystems, catalog no. KK8504) and Kapa UDI Adaptor Kit (Kapa Biosystems, catalog no. KK8727) according to manufacturer's protocol with the modifications described below. A-tailing temperature was reduced to 50°C to avoid melting of short DNA fragments and reaction time was increased to 1 h to compensate for reduced enzyme activity as described previously⁵². After the adapter ligation step, three consecutive rounds of Ampure purification were performed using a 1.4× bead:sample ratio to remove excess unligated adaptors while retaining short adapter-ligated fragments. Libraries were amplified for an average of 15 cycles using a 10-s, 60-°C annealing/extension step to enrich for shorter library fragments. After amplification, libraries were purified using three consecutive rounds of Ampure purification with a 1.2× bead:sample ratio to remove amplified primer dimers while retaining short library fragments. A 0.5× Ampure purification step was included to remove large fragments before sequencing. After PicoGreen quantification and quality control by Agilent BioAnalyzer, libraries were pooled equimolar and run on a HiSeq 4000 in a PE50 run, using the HiSeq 3000/4000 SBS Kit (Illumina). The loading concentration was 2 nM and a 5% spike-in of PhiX was added to the run to increase diversity and for quality control purposes.

Computational analysis of sequencing data. Alignment of F1 allele-specific reads. The F1 allele-specific reads were obtained from high-throughput sequencing experiments, including ATAC-seq, RNA-seq and CUT&RUN. Raw sequencing reads were run through the previously described diploid genome alignment pipeline¹⁶. Briefly, to ensure unbiased mapping of sequencing reads from F1 mice, a pseudo-Cast genome was constructed by modifying the B6 reference genome (GRCm38) with genetic polymorphisms detected in the wild-derived inbred CAST/Eij strain⁵³. Next, the sequencing reads were aligned to the B6 and the pseudo-Cast genome in parallel and the genomic coordinates of pseudo-Cast genome-aligned reads were converted back to B6 coordinates. The allelic origin of each variant-containing read was determined based on the CIGAR string and alignment scores. For reads mapped to exactly the same location, the alignment with a higher score was retained. For the nonvariant-containing reads, the diploid genome alignment yielded identical scores on both genomes, so one of the alignments was selected randomly. With this strategy, the final alignment file contains allele-specific reads that are assigned to either B6 or Cast alleles, as well as invariant reads that do not carry allelic origin information.

RNA-seq data analysis. The pseudo-Cast genome was transformed from GRCm38 by incorporating high-quality strain-specific variants (score ≥ 228). The RNA-seq data of naive and activated T cells were aligned using STAR⁵⁴, implemented in the diploid genome analysis pipeline with the following parameter settings: \$STAR --runMode alignReads --readFilesCommand zcat --outSAMtype BAM --outFilterMultimapNmax 1 --outFilterMatchNmin 30 --alignIntronMin 20 --alignIntronMax 20000 --alignEndsType Local. Allelic ratio of gene expression was obtained by counting the allele-specific read pileup allocated to genes. The gene annotation GTF file was downloaded from the ENSEMBL database at [ftp://ensembl.org/ensembl/pub/release-83/gtf](http://ensembl.org/ensembl/pub/release-83/gtf). Plots were generated using Graphpad Prism or R.

ATAC-seq data analysis. Similar to RNA-seq, the ATAC-seq data of naive and activated T cells were aligned using STAR⁵⁴ with the splicing alignment feature switched off. The chromatin-accessible peaks were called using MACS2 (model-based analysis of ChIP-seq 2)⁵⁵: \$macs2 call peak -t \$inputFile -f BED -n \$outputDir -g mm -p 1e-2 --nomodel --shift 75 --extsize 200 --keep-dup all --call-summits. The irreproducible discovery rate (IDR) procedure was used to evaluate the peak reproducibility among replicates⁵⁶. After removing the

irreproducible peaks (IDR value <0.05), the chromatin accessibility atlas was constructed by aggregating all the reproducible peaks from naive and activated cell types. For each accessible peak, the nearest gene was assigned, and the peak was further categorized as promoter, intronic, exonic and intergenic *cis*-elements, respectively. Plots were generated using Graphpad Prism or R.

CUT&RUN data analysis. The paired-end CUT&RUN data of different transcription factors were mapped to the diploid genome using STAR⁵⁴ with the splicing alignment feature switched off: \$STAR --runMode alignReads --readFilesCommand zcat --outSAMtype BAM SortedByCoordinate --outFilterMultimapNmax 1 --outFilterMatchNmin 40 --outFilterMatchNminOverLread 0.4 --seedSearchStartLmax 15 --alignIntronMax 1 --alignEndsType Local. The aligned read pairs were retained if the fragment length was between 50 and 500 bp. Reads aligned to multiple loci were removed from further analysis. Peaks were called using MACS2 with its --nomodel setting⁵⁵. The IDR procedure was used to evaluate the peak reproducibility as described above⁵⁶. A peak atlas was generated for individual TFs by retaining the reproducible peaks (IDR < 0.2). CUT&RUN peaks that do not overlap ATAC-seq peaks were removed from the atlas. Plots were generated using Graphpad Prism or R.

Identification of active TF-binding motifs. Experimentally determined *Mus musculus* motifs identified by chromatin immunoprecipitation sequencing (ChIP-seq), PBM, SELEX or HocoMoco were retrieved from the CIS-BP database⁵⁷. The motif position weight matrix was scanned using FIMO⁵⁸ against the target peak sequences of both alleles for ATAC-seq and CUT&RUN data with default parameters. For motifs containing genetic variants, the degree of motif match on the B6 and Cast alleles was determined based on the significance of the FIMO *P* value. For a given TF-binding motif, the match strength was subsequently associated with the allelic imbalance of peaks containing the particular motif genome wide. Peaks containing fewer than ten allele-specific reads were excluded from this analysis. A two-sided Student's *t*-test was used to determine whether a stronger motif match on B6 or Cast alleles was associated with allelic imbalance of TF-binding intensity or chromatin accessibility.

TF-binding motif enrichment analysis. The same motifs used for identifying active TF-binding motifs were identified within the peak sets of interest and background peaks using FIMO⁵⁸ as described above. We defined a peak containing a motif if the motif resides within a distance of 300 bp from the peak summit. The nonparametric Fisher's exact test was used to identify the motifs enriched in the target peak group.

ScATAC-seq analysis. For the scATAC experiment, total CD4 and CD8 T cells were sorted from pooled splenocytes of three LCMV Armstrong-infected (B6/Cast) F1 mice on day 7 post-infection. Sorted CD4 and CD8 T cells were mixed at equal ratios and used as input material for scATAC-seq analysis. Libraries were prepared according to the 10× scATAC-seq protocol from 10× Genomics Chromium (Single Cell ATAC Reagent Kits User Guide (catalog no. CG000168, Rev A)). Briefly, cells were centrifuged (300g, 5 min, 4 °C) and permeabilized with 100 µl of chilled lysis buffer (10 mM Tris-HCl, pH 7.4, 10 mM NaCl, 3 mM MgCl₂, 0.1% Tween-20, 0.1% IGEPAL CA-630, 0.01% digitonin and 1% bovine serum albumin). The sample was incubated on ice for 3–5 min and resuspended with 1 ml of chilled wash buffer (10 mM Tris-HCl, pH 7.4, 10 mM NaCl, 3 mM MgCl₂, 0.1% Tween-20 and 1% bovine serum albumin). After centrifugation (500g, 5 min, 4 °C), the pellet was resuspended in 100 µl of chilled Nuclei Buffer (catalog no. 2000153, 10× Genomics). Nuclei were counted using a hemocytometer, and finally the nucleus concentration was adjusted to 3,000 nuclei per µl. We used 15,360 nuclei as input for fragmentation. Nuclei were diluted to 5 µl with 1× Nuclei Buffer (10× Genomics) and mixed with ATAC buffer (10× Genomics) and ATAC enzyme (10× Genomics) for fragmentation (60 min, 37 °C). ScATAC-seq libraries were generated using the Chromium Chip E Single Cell ATAC kit (10× Genomics, catalog no. 1000086) and indices (Chromium i7 Multiplex Kit N, Set A, 10× Genomics, catalog no. 1000084) following the manufacturer's instructions. Final libraries were quantified using a Qubit fluorimeter (Life Technologies) and the nucleosomal pattern was verified using a BioAnalyzer (Agilent). Libraries were sequenced on a NovaSeq6000 (Illumina) with the following read lengths: 50 + 8 + 16 + 50 (Read 1 + Index 1 + Index 2 + Read 2).

ScATAC-seq data were aligned to the hybrid mouse genome using the following strategy: files CAST_Eij.mgp.v5.snps.dbSNP142.vcf and CAST_Eij.mgp.v5.indels.dbSNP142.normed.vcf with SNP and indel genetic variants between B6 and Cast genomes were obtained from the Mouse Genome Project⁵³. MMARGE v.1.0 (ref. ⁵⁹) was used to create a Cast pseudogenome by introducing all variants to the B6 genome. Gene annotations were obtained from GENCODE v.M25 (ref. ⁶⁰) and mapped from B6 to Cast genomic coordinates using MMARGE (motif mutation analysis for regulatory genomic elements). ScATAC-seq read alignment and preprocessing were done using cellranger-atac v.1.2.0. For this, cellranger-atac mkref was used to create customized B6 and Cast references, and cellranger-atac count was used for alignment. Cast alignments were then mapped to B6 coordinates using MMARGE. Customized script was used to identify each read

in both B6 and Cast alignments and declared the read B6 or Cast specific if the alignment score was higher for that allele, and the read ambiguous if the two scores were equal. In this procedure, reads were treated as single-end. The cellranger-atac was also used with the default mm10 reference redata-cellranger-atac-mm10-1.2.0 for allele-agnostic scATAC-seq alignment.

ArchR v.1.0.1 (ref. ⁶¹) was used for the allele-agnostic scATAC-seq analysis. The data were preprocessed by removing cells with counts <7,500 and >1 × 10⁵, and filtering out doublets with a doublet enrichment score >2.0. Then the count matrix was generated using a tile size of 500 bp, without binarizing the counts. After preliminary analysis, 17 cells were classified as probably B cells, based on their high accessibility at genes *Cd79a*, *Cd79b* and low accessibility at *Cd3g*, and removed from the analysis. The resulting count matrix for 6,043 cells was used for subsequent analysis. LSI (latent semantic indexing) dimensionality reduction was performed with 4 iterations, maximum cluster size of 25 and resolution of 1.5, and the number of variable features equal to 52,004 (matching the number of peaks obtained from bulk ATAC-seq analysis) and otherwise default parameters. Clustering was performed with resolution 2.0 and otherwise default parameters. UMAP (Uniform Manifold Approximation and Projection) was generated with the parameters nNeighbors = 30, minDist = 0.5 and spread = 3. Clusters were annotated with cell states based on ArchR gene scores for a selection of marker genes. Scores for each peak group defined using bulk ATAC-seq and CUT&RUN analysis were generated using the scATAC-seq peak matrix generated with ArchR (allowing up to a read count of 30 per peak per cell). For each cell, peak counts were summed over all peaks in the peak group and then divided by the total number of counts over all peaks in the cell to generate a peak group score.

Allele-specific scATAC-seq counts were calculated for peaks obtained from bulk ATAC-seq analysis. For each peak in each cell, reads with the same start and end positions that aligned to that peak were collapsed to avoid PCR duplicates. For cell states annotated in the above analysis, allele-specific pseudo-bulk count matrices were generated by summing the allele-specific counts for each peak across all cells within each cell state.

Statistics and reproducibility. No statistical method was used to predetermine sample size. No data were excluded from the analyses. The experiments were not randomized. The investigators were not blinded to allocation during experiments and outcome assessment.

Reporting Summary. Further information on research design is available in the Nature Research Reporting Summary linked to this article.

Data availability

All next-generation sequencing data generated in this paper were deposited in the Gene Expression Omnibus under SuperSeries accession nos, GSE166718 and GSE184006. Processed data are included with the manuscript as supplementary tables. The B6 reference genome (GRCm38) was downloaded from the National Center for Biotechnology Information. Files CAST_Eij.mgp.v5.snps.dbSNP142.vcf and CAST_Eij.mgp.v5.indels.dbSNP142.normed.vcf with SNP and indel genetic variants between B6 and Cast genomes were obtained from the Mouse Genome Project⁵³. Gene annotations were downloaded from the ENSEMBL database at [ftp://ensembl.org/ensembl/pub/release-83/gtf](http://ensembl.org/ensembl/pub/release-83/gtf) or obtained from GENCODE v.M5 (ref. ⁶⁰). Experimentally determined *Mus musculus* motifs identified by ChIP-seq, PBM, SELEX or HocoMoco were retrieved from the CIS-BP database⁵⁷.

Code availability

The customized Shell and Python code used in the present study is publicly available at the MSKCC website: <http://cbio.mskcc.org/public/Leslie/zhongy/downloads/index8.html>

References

50. Buenrostro, J. D., Giresi, P. G., Zaba, L. C., Chang, H. Y. & Greenleaf, W. J. Transposition of native chromatin for fast and sensitive epigenomic profiling of open chromatin, DNA-binding proteins and nucleosome position. *Nat. Methods* **10**, 1213–1218 (2013).
51. Skene, P. J. & Henikoff, S. An efficient targeted nuclease strategy for high-resolution mapping of DNA binding sites. *eLife* <https://doi.org/10.7554/eLife.21856> (2017).
52. Liu, N. et al. Direct promoter repression by BCL11A controls the fetal to adult hemoglobin switch. *Cell* **173**, 430–442.e417 (2018).
53. Keane, T. M. et al. Mouse genomic variation and its effect on phenotypes and gene regulation. *Nature* **477**, 289–294 (2011).
54. Dobin, A. et al. STAR: ultrafast universal RNA-seq aligner. *Bioinformatics* **29**, 15–21 (2013).
55. Zhang, Y. et al. Model-based analysis of ChIP-Seq (MACS). *Genome Biol.* **9**, R137 (2008).
56. Li, Q., Brown, J. B., Huang, H. & Bickel, P. J. Measuring reproducibility of high-throughput experiments. *Ann. Appl. Stat.* **5**, 1752–1779 (2011).

57. Weirauch, M. T. et al. Determination and inference of eukaryotic transcription factor sequence specificity. *Cell* **158**, 1431–1443 (2014).
58. Grant, C. E., Bailey, T. L. & Noble, W. S. FIMO: scanning for occurrences of a given motif. *Bioinformatics* **27**, 1017–1018 (2011).
59. Link, V. M., Romanoski, C. E., Metzler, D. & Glass, C. K. MMARGE: motif mutation analysis for regulatory genomic elements. *Nucleic Acids Res.* **46**, 7006–7021 (2018).
60. Frankish, A. et al. GENCODE reference annotation for the human and mouse genomes. *Nucleic Acids Res.* **47**, D766–D773 (2019).
61. Granja, J. M. et al. ArchR is a scalable software package for integrative single-cell chromatin accessibility analysis. *Nat. Genet.* **53**, 403–411 (2021).

Acknowledgements

We thank all members of the Rudensky lab for discussions and technical assistance. We thank the NIH tetramer core for providing critical reagents. The present study was supported by NIH grants (nos. R01AI034206, U54 CA209975) and NIH/National Cancer Institute (NCI, grant no. P30 CA008748), AACR-Bristol-Myers Squibb Immuno-oncology Research Fellowship (no. 19-40-15-PRIT), National Natural Science Foundation of China (grant no. 32170883 to Y.Z.), the Ludwig Center at MSKCC and the Parker Institute for Cancer Immunotherapy. A.Y.R. is an investigator with the Howard Hughes Medical Institute. We acknowledge the use of the MSKCC Single Cell Research Initiative and the Integrated Genomics Operation Core, funded by the NIH/NCI Cancer Center Support (grant no. P30 CA008748), Cycle for Survival, and the Marie-Josée and Henry R. Kravis Center for Molecular Oncology.

Author contributions

J.v.d.V. and A.Y.R. designed the study. J.v.d.V. performed the experiments and analyzed the data. Y.Z. and C.S.L. designed the allele-specific analysis pipeline. Y.Z. performed the computational analysis of sequencing data. S.K.W. and Y.P. analyzed the scATAC-seq data. J.v.d.V. and A.Y.R. wrote the manuscript with input from all authors.

Competing interests

A.Y.R. is an SAB member, has equity in Sonoma Biotherapeutics and Vedanta Biosciences, and is a co-inventor or has IP licensed to Takeda that is unrelated to the content of the present study. The remaining authors declare no competing interests.

Additional information

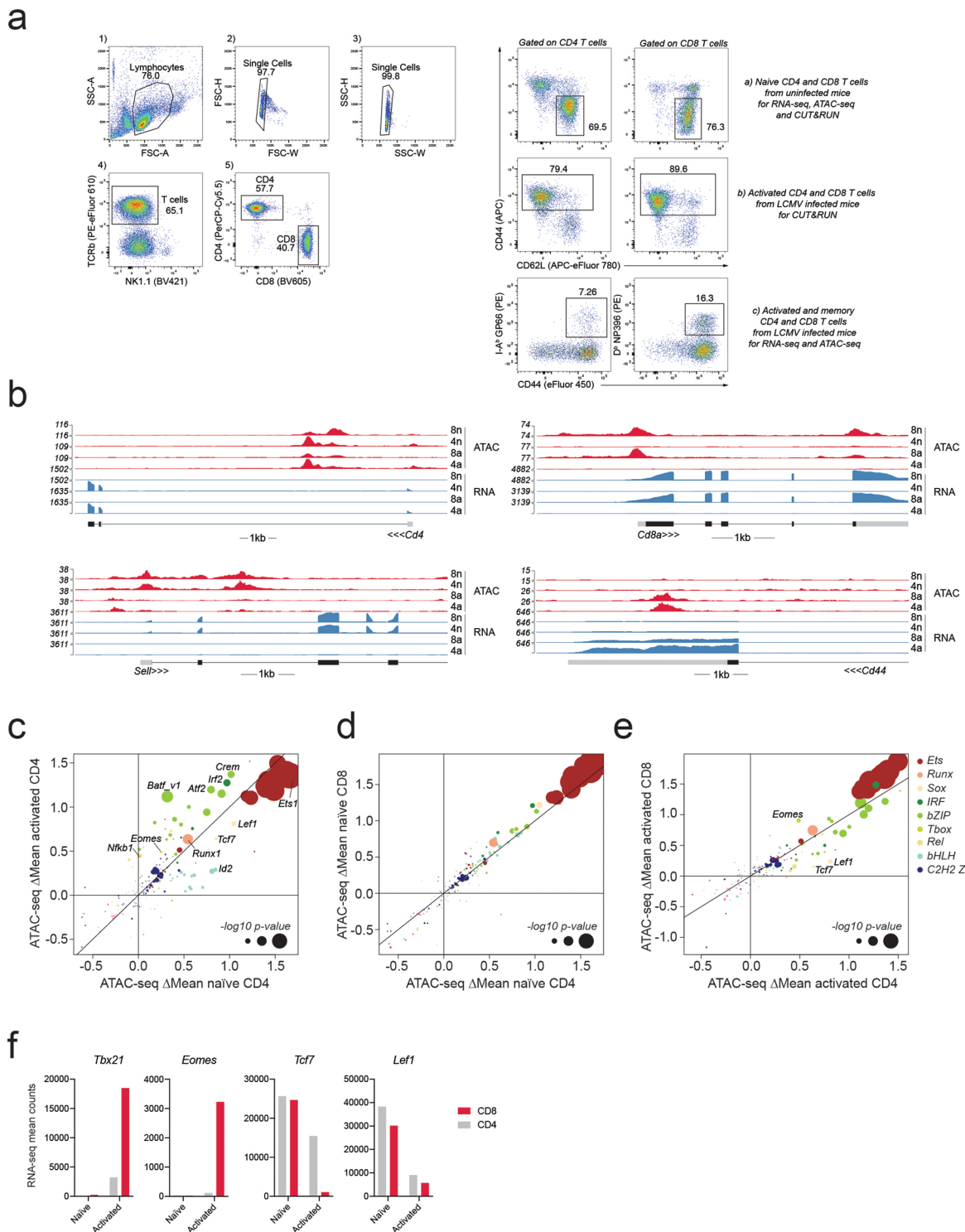
Extended data Extended data are available for this paper at <https://doi.org/10.1038/s41590-021-01086-x>.

Supplementary information The online version contains supplementary material available at <https://doi.org/10.1038/s41590-021-01086-x>.

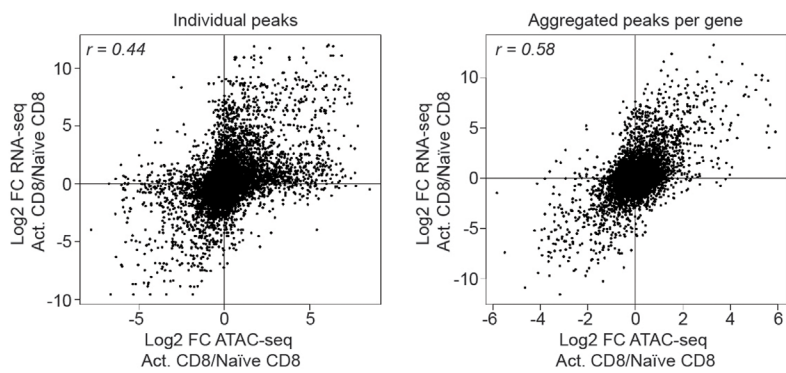
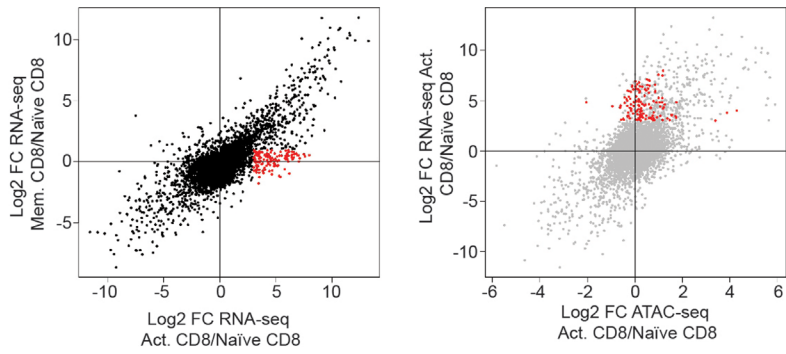
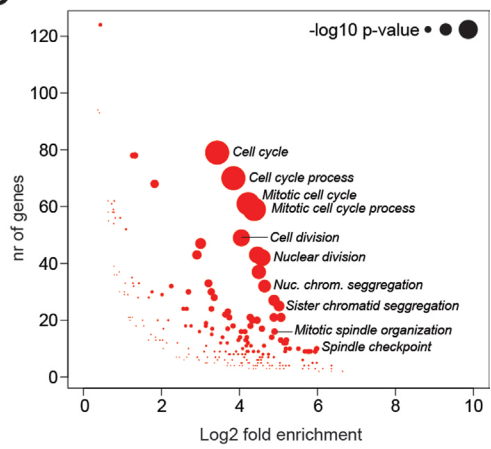
Correspondence and requests for materials should be addressed to Alexander Y. Rudensky or Joris van der Veeken.

Peer review information Peer review reports are available. L. A. Dempsey was the primary editor on this article and managed its editorial process and peer review in collaboration with the rest of the editorial team.

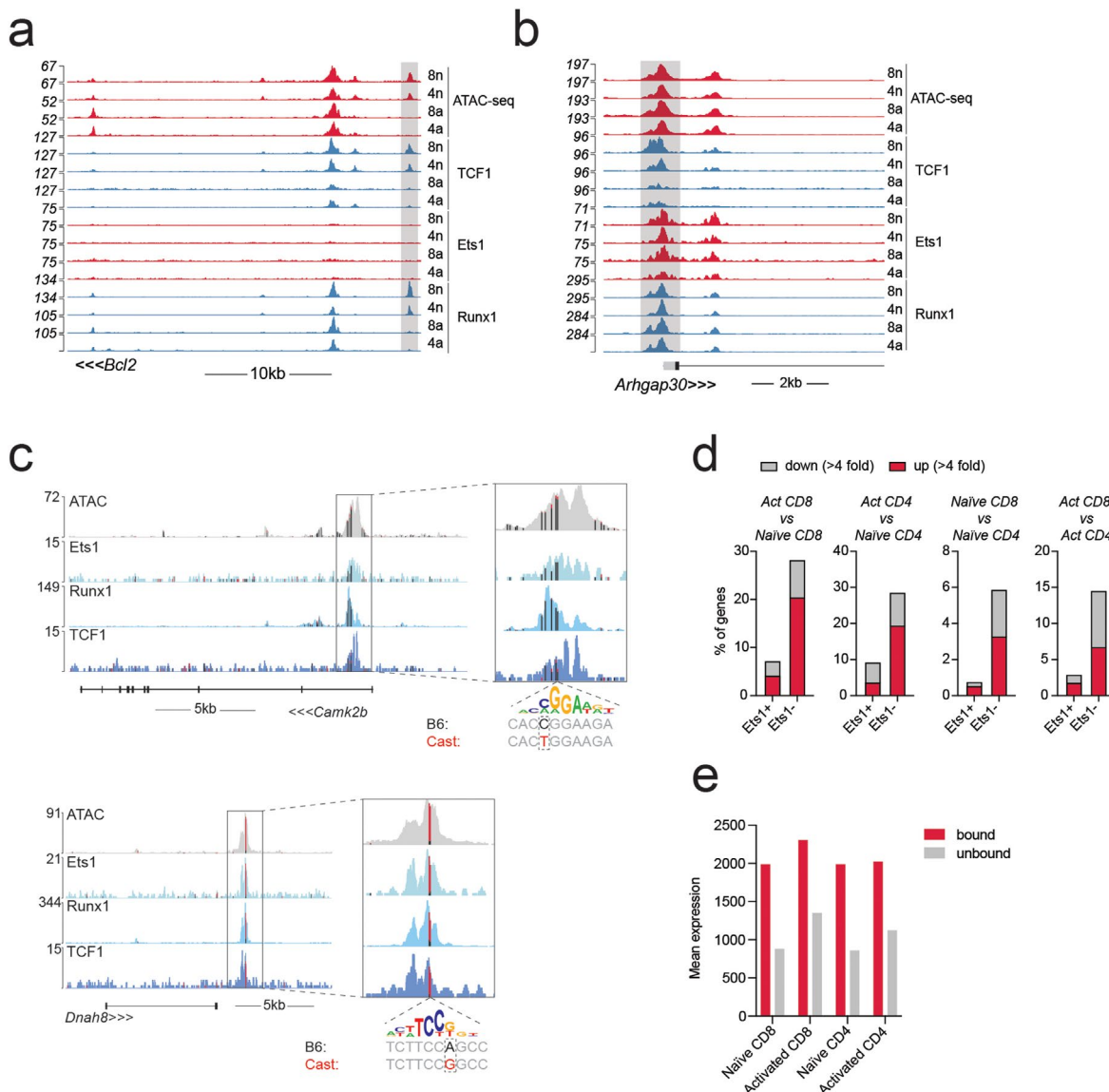
Reprints and permissions information is available at www.nature.com/reprints.



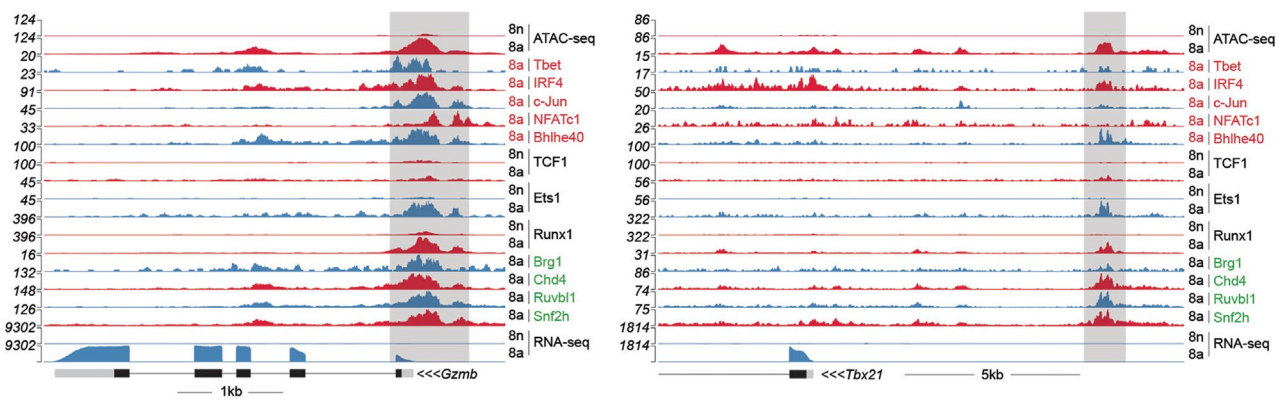
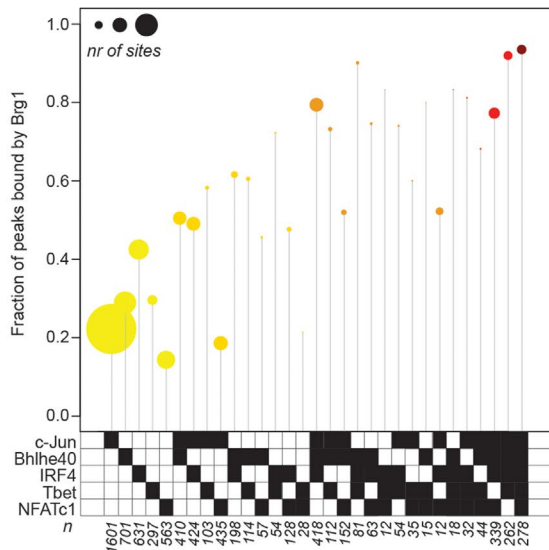
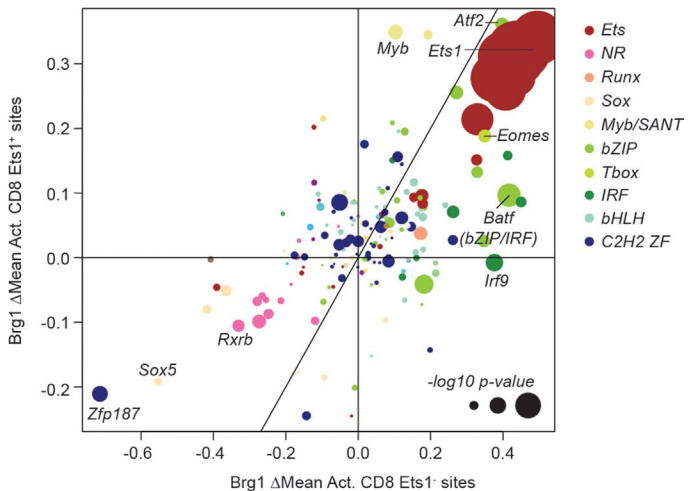
Extended Data Fig. 1 | RNA-seq and ATAC-seq of naive and activated CD4 and CD8 T cells. **a:** Example of gating strategy for cell isolation from the spleen. Live lymphocytes were identified based on FSC-A/SSC-A. Doublets were gated out and CD4 and CD8 T cells were identified as TCR β^+ CD4 $^+$ and TCR β^+ CD8 $^+$, respectively. Naive CD4 and CD8 T cells used as input for RNA-seq, ATAC-seq, and CUT&RUN experiments were isolated from uninfected mice as CD44 $^+$ CD62L $^-$ cells. Bulk activated CD4 and CD8 T cells used as input for CUT&RUN experiments were isolated as CD44 $^+$ cells from LCMV Armstrong infected mice on day 7–8 post-infection (p.i.). LCMV-specific activated and memory CD4 and CD8 T cells used as input for ATAC-seq and RNA-seq experiments were isolated based on tetramer staining on day 7 or day 60 p.i. **b:** RNA-seq and ATAC-seq reads at the *Cd4*, *Cd8a*, *Sell* and *Cd44* loci in naive and activated CD4 and CD8 T cells. **c-e:** Effect of TF binding motif variants on chromatin accessibility measured as Δ Mean in naive and activated CD4 T cells (A), naive CD4 and CD8 T cells (B), activated CD4 and CD8 T cells (C). Data points are colored by TF family and scaled according to the $-\log_{10}$ p-value of a two-sided t-test comparing the mean allelic ratios between peaks with stronger matches on the B6 vs Cast allele. The most significant p-value obtained across the two cell types (naive and activated CD8) was used for scaling. Motifs with <50 variant-containing motif occurrences were excluded from the plot. **f:** Mean RNA-seq counts for *Tbx21*, *Eomes*, *Tcf7* and *Lef1* in naive and activated CD4 and CD8 T cells.

a**b****c**

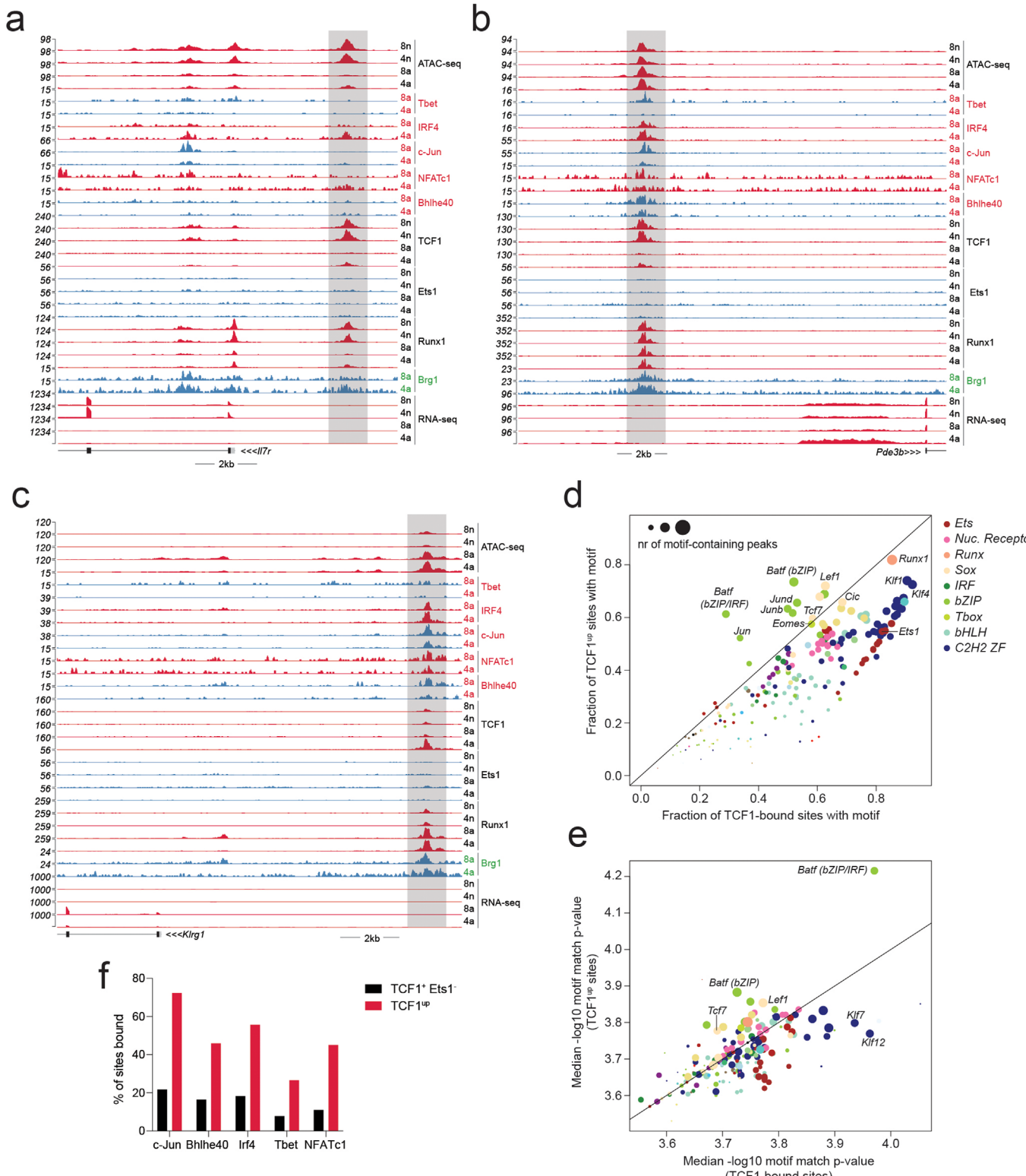
Extended Data Fig. 2 | Association between gene expression and chromatin accessibility changes. **a:** Correlation between changes in chromatin accessibility and gene expression in activated vs naïve CD8 T cells. Showing individual ATAC-seq peaks linked to the nearest gene (left) or the sum of counts across all ATAC-seq peaks linked to the same gene (right). **b:** Fold change in gene expression in activated vs naïve CD8 T cells (x-axis) plotted against the fold change in gene expression in memory vs naïve CD8 T cells (y-axis). A subset of genes whose expression is transiently induced upon T cell activation is highlighted in red (left). Aggregated chromatin accessibility and gene expression changes for this gene set (right). **c:** Gene ontology (GO) term enrichment analysis on genes highlighted in panel B.



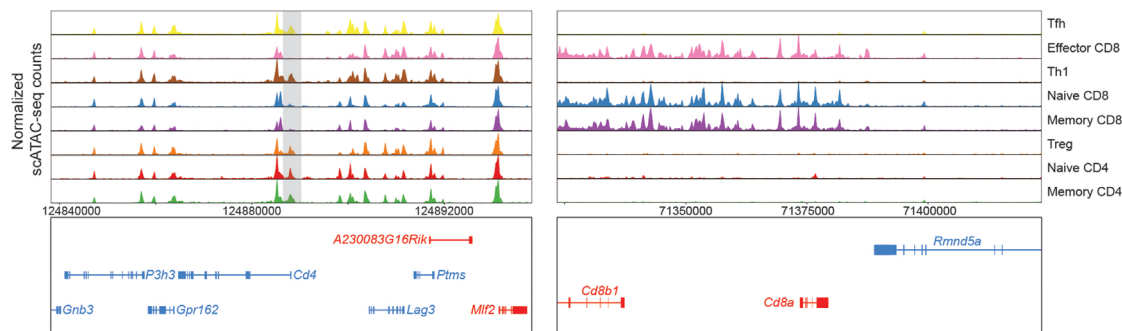
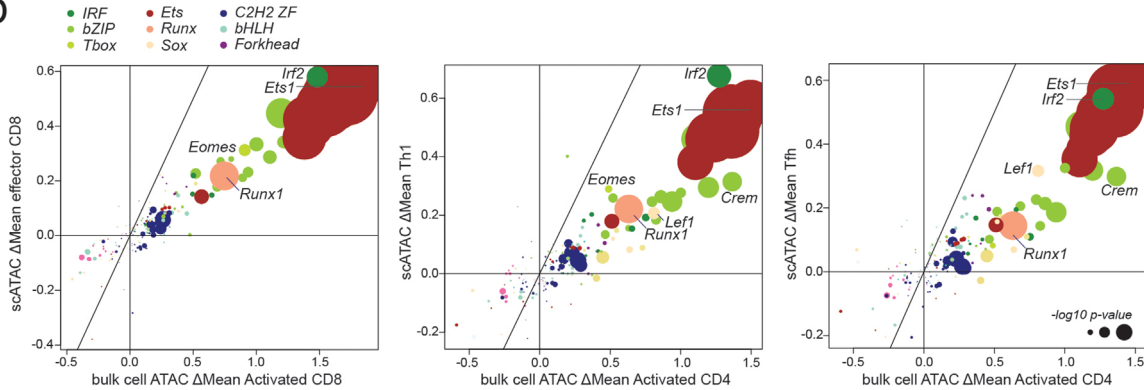
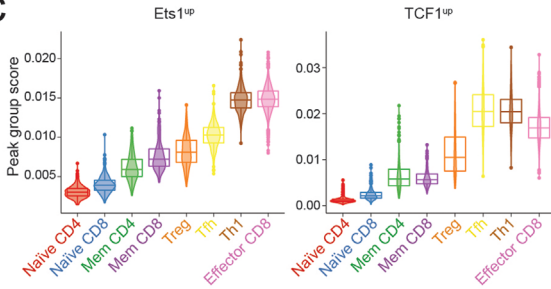
Extended Data Fig. 3 | RNA-seq and ATAC-seq changes at Runx1, TCF1, and Ets1-bound genes. **a-b:** Gene tracks of RNA-seq, ATAC-seq and CUT&RUN coverage at the *Bcl2* and *Arhgap30* loci in naive and activated CD8 T cells. **c:** Track examples showing the effect of selected Ets1 motif variants on allelic bias in chromatin accessibility and TF binding in activated CD8 T cells from (B6/Cast) F1 mice. Vertical bars mark the position of genetic variants, with colors indicating the fraction of variant-containing reads coming from either the B6 (black) or Cast (red) allele. A genetic variant in the *Camk2b* locus results in a stronger Ets1 motif match on the B6 allele and a weaker match on the Cast allele and is associated with B6-specific chromatin accessibility and TF binding. The opposite pattern is observed at the *Dnah8* locus. **d:** Gene expression changes at genes (>100 reads in at least one cell type) nearest to Ets1-bound and -unbound ATAC-seq peaks. **e:** Mean expression of genes nearest to Ets1-bound and -unbound ATAC-seq peaks.

a**b****c**

Extended Data Fig. 4 | TF and cofactor binding at Ets1-bound and -unbound chromatin regions. a: Gene tracks of RNA-seq, ATAC-seq and CUT&RUN coverage at the *Gzmb* and *Tbx21* loci in naive and activated CD8 T cells. **b:** Fraction of peaks bound by Brg1 at Ets1-unbound ATAC-seq peaks occupied by distinct combinations of activation-induced TFs. Data points are scaled according to the number of peaks in each set. **c:** Effect of TF binding motif variants on Brg1 occupancy at Ets1-bound (*Ets1*⁺) and Ets1-unbound (*Ets1*⁻) sites measured as ΔMean in activated CD8 T cells. Data points are colored by TF family and scaled according to the $-\log_{10} p\text{-value}$ of a t-test comparing the allelic ratios between peaks with stronger motif matches on the B6 vs Cast allele. The most significant p-value obtained across the two cell types (naive and activated CD8) was used for scaling.



Extended Data Fig. 5 | TF binding at TCF1-bound peak sets in naïve and activated CD4 and CD8 T cells. **a-c:** Gene tracks of RNA-seq, ATAC-seq and CUT&RUN read coverage at the *II7r*, *Pde3b* and *Klr1g* loci in naïve and activated CD4 and CD8 T cells. **d:** Fraction of TCF1-bound sites and TCF1^{up} sites containing specific TF-binding motifs. **e:** Median motif match p-value at sites bound at TCF1-bound sites and TCF1^{up} sites. **f:** Percentage of TCF1+ Ets1- peaks and TCF1^{up} peaks bound by each activation-induced TF.

a**b****c**

Extended Data Fig. 6 | Single cell ATAC-seq analysis of T cell subsets during acute LCMV infection. **a:** Pseudo-bulk scATAC-seq tracks showing chromatin accessibility at CD4 and CD8 loci across splenic cell populations in LCMV infected (B6/Cast) F1 mice. **b:** Effect of genetic variation in TF binding motifs on allele-specific ATAC-seq counts from bulk cell or single cell experiments. Data points are colored by TF family and scaled according to the $-\log_{10}$ p-value of a two-sided t-test comparing the allelic ratios between peaks with stronger matches on B6 vs Cast Allele. **c:** Violin plots and box plots showing accessibility of indicated peak groups across T cell subsets. The center line in the box plots represents the median, the box limits represent the 25th and 75th percentiles, and the whiskers are the minimum/maximum values within 1.5 times the interquartile range. $n =$ the number of cells in each cell annotation (420 Naive CD4, 344 Naive CD8, 234 Mem CD4, 231 Mem CD8, 198 Treg, 1321 Th1, 652 Th1, 2583 Effector CD8).

Reporting Summary

Nature Research wishes to improve the reproducibility of the work that we publish. This form provides structure for consistency and transparency in reporting. For further information on Nature Research policies, see our [Editorial Policies](#) and the [Editorial Policy Checklist](#).

Statistics

For all statistical analyses, confirm that the following items are present in the figure legend, table legend, main text, or Methods section.

n/a Confirmed

- The exact sample size (n) for each experimental group/condition, given as a discrete number and unit of measurement
- A statement on whether measurements were taken from distinct samples or whether the same sample was measured repeatedly
- The statistical test(s) used AND whether they are one- or two-sided
Only common tests should be described solely by name; describe more complex techniques in the Methods section.
- A description of all covariates tested
- A description of any assumptions or corrections, such as tests of normality and adjustment for multiple comparisons
- A full description of the statistical parameters including central tendency (e.g. means) or other basic estimates (e.g. regression coefficient) AND variation (e.g. standard deviation) or associated estimates of uncertainty (e.g. confidence intervals)
- For null hypothesis testing, the test statistic (e.g. F , t , r) with confidence intervals, effect sizes, degrees of freedom and P value noted
Give P values as exact values whenever suitable.
- For Bayesian analysis, information on the choice of priors and Markov chain Monte Carlo settings
- For hierarchical and complex designs, identification of the appropriate level for tests and full reporting of outcomes
- Estimates of effect sizes (e.g. Cohen's d , Pearson's r), indicating how they were calculated

Our web collection on [statistics for biologists](#) contains articles on many of the points above.

Software and code

Policy information about [availability of computer code](#)

Data collection FACS Diva v 8.0 (BD) for flow cytometry. HCS 3.4.0 (Illumina) for HiSeq 4000.

Data analysis Flowjo 10.7.1, Graphpad Prism v9.0.0, custom R scripts for plotting, STAR v2.5.0c, MACS2 v2.1.1, custom python code to build diploid genome, align and call allele-specific reads and perform motif analysis. MMARGE v1.0, cellranger-atac v1.2.0 and ArchR v1.0.1 were used for scATAC-seq analysis. The custom Shell and Python code used in this study are publicly available at Memorial Sloan Kettering Cancer Center website: http://cbio.mskcc.org/public/Leslie_zhongy/downloads/index8.html

For manuscripts utilizing custom algorithms or software that are central to the research but not yet described in published literature, software must be made available to editors and reviewers. We strongly encourage code deposition in a community repository (e.g. GitHub). See the Nature Research [guidelines for submitting code & software](#) for further information.

Data

Policy information about [availability of data](#)

All manuscripts must include a [data availability statement](#). This statement should provide the following information, where applicable:

- Accession codes, unique identifiers, or web links for publicly available datasets
- A list of figures that have associated raw data
- A description of any restrictions on data availability

All next generation sequencing data generated in this paper were deposited in the Gene Expression Omnibus (GEO) under SuperSeries accession numbers GSE166718 and GSE184006. Processed data are included with the manuscript as supplemental tables. The B6 reference genome (GRCm38) was downloaded from NCBI. Files CAST_Eij.mgp.v5.snps.dbSNP142.vcf and CAST_Eij.mgp.v5.indels.dbSNP142.normed.vcf with SNP and indel genetic variants between B6 and Cast genomes were obtained from the Mouse Genome Project60. Gene annotations were downloaded from ENSEMBL database at <ftp.ensembl.org/ensembl/pub/>

Field-specific reporting

Please select the one below that is the best fit for your research. If you are not sure, read the appropriate sections before making your selection.

Life sciences Behavioural & social sciences Ecological, evolutionary & environmental sciences

For a reference copy of the document with all sections, see nature.com/documents/nr-reporting-summary-flat.pdf

Life sciences study design

All studies must disclose on these points even when the disclosure is negative.

Sample size	No statistical methods were used to predetermine sample size. Sample sizes were determined by availability of mice and requirements for input material
Data exclusions	No data were excluded
Replication	Biological replicates were used for all sequencing experiments. The number of reproducible peaks in each experiment is listed in the supplemental data table. Sequencing experiments were not technically replicated.
Randomization	Mice were randomly assigned to experimental groups.
Blinding	Investigators were not blinded during group allocation and data analysis because infection status of the mice immediately apparent during sample processing and analysis.

Reporting for specific materials, systems and methods

We require information from authors about some types of materials, experimental systems and methods used in many studies. Here, indicate whether each material, system or method listed is relevant to your study. If you are not sure if a list item applies to your research, read the appropriate section before selecting a response.

Materials & experimental systems		Methods	
n/a	Involved in the study	n/a	Involved in the study
<input type="checkbox"/>	<input checked="" type="checkbox"/> Antibodies	<input type="checkbox"/>	<input checked="" type="checkbox"/> ChIP-seq
<input checked="" type="checkbox"/>	<input type="checkbox"/> Eukaryotic cell lines	<input type="checkbox"/>	<input checked="" type="checkbox"/> Flow cytometry
<input checked="" type="checkbox"/>	<input type="checkbox"/> Palaeontology and archaeology	<input checked="" type="checkbox"/>	<input type="checkbox"/> MRI-based neuroimaging
<input type="checkbox"/>	<input checked="" type="checkbox"/> Animals and other organisms		
<input checked="" type="checkbox"/>	<input type="checkbox"/> Human research participants		
<input checked="" type="checkbox"/>	<input type="checkbox"/> Clinical data		
<input checked="" type="checkbox"/>	<input type="checkbox"/> Dual use research of concern		

Antibodies

Antibodies used	The following antibodies were used for CUT&RUN experiments Runx1 (Thermo Fisher; PA5-19638, polyclonal, lot TC2546282) TCF1 (Cell Signaling Technology; 2203S, clone C63D9, lot 7) Ets1 (Cell Signaling Technology; 14069, clone D808A, lot 1) T-bet (Santa Cruz Biotechnology; sc-21003 X; polyclonal, lot C2715) IRF4 (Santa Cruz Biotechnology; sc-6059; polyclonal, lot J2015) c-Jun (Abcam; ab31419; polyclonal, lot GR306615-13) NFATc1 (Biolegend; 649607; clone 7A6, lot B251075) Bhlhe40 (Novus Biologicals; NB100-1800SS; polyclonal, lot c3) Brg1 (Abcam; ab110641; EPNCIR111A, lot GR3208604-19) Chd4 (Abcam; ab72418; polyclonal, lot GR300277-33) Ruvbl1 (Proteintech group; 10210-2-AP; polyclonal, lot 00045851) Snf2h (Abcam; ab3749; polyclonal, lot GR3246671-1) CD45 – Alexa Fluor 700 (ThermoFisher; 56-0451-82; clone 30F-11) TCRβ – PE-ef610 (ThermoFisher; 61-5961-82; clone H57-597) CD4 – Percp-Cy5.5 (Tonbo Bioscience; 65-0042-U100; clone RM4-5) CD8a – BV605 (BioLegend; 100744; clone 53-6.7) CD44 – APC (Tonbo Bioscience; 20-0441-U100; clone IM7)
-----------------	--

CD44 – ef450 (ThermoFisher; 48-0441-82; clone IM7)
 CD62L – APC-ef780 (ThermoFisher; 47-0621-82; clone Mel-14)
 NK1.1 – ef450 (ThermoFisher; 48-5941-82; clone PK136)

Validation

Antibodies are commercially available and were validated by the respective manufacturers. Please refer to the spec sheets on the vendor's websites for technical information by searching with the catalog numbers provided. Specificity of transcription factor (TF) antibodies in CUT&RUN is further supported by analysis of TF binding motif analysis.

Animals and other organisms

Policy information about [studies involving animals](#); [ARRIVE guidelines](#) recommended for reporting animal research

Laboratory animals

Animals were housed at the Memorial Sloan Kettering Cancer Center (MSKCC) animal facility under specific pathogen free (SPF) conditions on a 12-hour light/dark cycle at an average ambient temperature of 21.5°C and average humidity of 48% with free access to food and water. Mice used in this study had no previous history of experimentation or exposure to drugs. Male Cast/Eij mice were purchased from Jackson Laboratory and bred to female B6 mice to generate F1 offspring. Adult mice (> 6 weeks old) were used for experiments.

Wild animals

No wild animals were used in the study

Field-collected samples

No field collected samples were used in the study

Ethics oversight

All studies were performed under protocol 08-10-023 and approved by the MSKCC Institutional Animal Care and Use Committee.

Note that full information on the approval of the study protocol must also be provided in the manuscript.

ChIP-seq

Data deposition

- Confirm that both raw and final processed data have been deposited in a public database such as [GEO](#).
- Confirm that you have deposited or provided access to graph files (e.g. BED files) for the called peaks.

Data access links

May remain private before publication.

GSE166718

Files in database submission

naive_cd4_rep1
 naive_cd4_rep2
 GP66_d7_rep1
 GP66_d7_rep2
 GP66_d60_rep1
 GP66_d60_rep2
 naive_cd8_rep1
 naive_cd8_rep2
 NP396_d7_rep1
 NP396_d7_rep2
 NP396_d60_rep1
 NP396_d60_rep2
 naive_cd4_rep1
 naive_cd4_rep2
 GP66_d7_rep1
 GP66_d7_rep2
 GP66_d60_rep1
 GP66_d60_rep2
 naive_cd8_rep1
 naive_cd8_rep2
 NP396_d7_rep1
 NP396_d7_rep2
 NP396_d60_rep1
 NP396_d60_rep2
 Runx1_naive_CD4_rep1
 Runx1_naive_CD4_rep2
 Runx1_activated_CD4_rep1
 Runx1_activated_CD4_rep2
 Runx1_naive_CD8_rep1
 Runx1_naive_CD8_rep2
 Runx1_activated_CD8_rep1
 Runx1_activated_CD8_rep2
 TCF1_Naive_CD4_rep1

TCF1_Naive_CD4_rep2
 TCF1_Activated_CD4_rep1
 TCF1_Activated_CD4_rep2
 TCF1_Naive_CD8_rep1
 TCF1_Naive_CD8_rep2
 TCF1_Activated_CD8_rep1
 TCF1_Activated_CD8_rep2
 Ets1_Naive_CD4_rep1
 Ets1_Naive_CD4_rep2
 Ets1_Activated_CD4_rep1
 Ets1_Activated_CD4_rep2
 Ets1_Naive_CD8_rep1
 Ets1_Naive_CD8_rep2
 Ets1_Activated_CD8_rep1
 Ets1_Activated_CD8_rep2
 Brg1_Activated_CD4_rep1
 Brg1_Activated_CD4_rep2
 Brg1_Activated_CD8_rep1
 Brg1_Activated_CD8_rep2
 Snf2h_Activated_CD4_rep1
 Snf2h_Activated_CD4_rep2
 Snf2h_Activated_CD8_rep1
 Snf2h_Activated_CD8_rep2
 Chd4_Activated_CD4_rep1
 Chd4_Activated_CD4_rep2
 Chd4_Activated_CD8_rep1
 Chd4_Activated_CD8_rep2
 Ruvbl1_Activated_CD4_rep1
 Ruvbl1_Activated_CD4_rep2
 Ruvbl1_Activated_CD8_rep1
 Ruvbl1_Activated_CD8_rep2
 cJun_Act_CD4_rep1
 cJun_Act_CD4_rep2
 cJun_Act_CD8_rep1
 cJun_Act_CD8_rep2
 Bhlhe40_Act_CD4_rep1
 Bhlhe40_Act_CD4_rep2
 Bhlhe40_Act_CD8_rep1
 Bhlhe40_Act_CD8_rep2
 Act_CD4_IRF4_pAG_rep1
 Act_CD4_IRF4_pAG_rep2
 Act_CD8_IRF4_pAG_rep1
 Act_CD8_IRF4_pAG_rep2
 CD4_rep_1_NFATc1
 CD8_rep_1_NFATc1
 CD4_rep_2_NFATc1
 CD8_rep_2_NFATc1
 Act_CD4_rep1
 Act_CD4_rep2
 Act_CD8_rep1
 Act_CD8_rep2

Genome browser session
 (e.g. [UCSC](#))

[https://genome.ucsc.edu/cgi-bin/hgTracks?](https://genome.ucsc.edu/cgi-bin/hgTracks?db=mm10&lastVirtModeType=default&lastVirtModeExtraState=&virtModeType=default&virtMode=0&nonVirtPosition=&position=chr10%3A118439379%2D118447559&hgsid=1032489289_F0Y1Tjq1E9HDDmXJJJevYuAhMWq)
 db=mm10&lastVirtModeType=default&lastVirtModeExtraState=&virtModeType=default&virtMode=0&nonVirtPosition=&position=chr10%3A118439379%2D118447559&hgsid=1032489289_F0Y1Tjq1E9HDDmXJJJevYuAhMWq

Methodology

Replicates

Experiments were performed with biological duplicates derived from 2-5 pooled spleens per replicate.

Sequencing depth

CUT&RUN samples were sequenced using a PE50 run. Sequencing depth ranged from 9134095 to 44802690 reads. Duplicate rates ranged from 0.080743 to 0.527084. Information for individual samples is provided as a supplemental table.

Antibodies

The following antibodies were used for CUT&RUN experiments

Runx1 (Thermo Fisher; PA5-19638, polyclonal, lot TC2546282)
 TCF1 (Cell Signaling Technology; 2203S, clone C63D9, lot 7)
 Ets1 (Cell Signaling Technology; 14069, clone D808A, lot 1)
 T-bet (Santa Cruz Biotechnology; sc-21003 X; polyclonal, lot C2715)
 IRF4 (Santa Cruz Biotechnology; sc-6059; polyclonal, lot J2015)
 c-Jun (Abcam; ab31419; polyclonal, lot GR306615-13)
 NFATc1 (Biolegend; 649607; clone 7A6, lot B251075)
 Bhlhe40 (Novus Biologicals; NB100-1800SS; polyclonal, lot c3)
 Brg1 (Abcam; ab110641; EPNCIR111A, lot GR3208604-19)
 Chd4 (Abcam; ab72418; polyclonal, lot GR300277-33)

Ruvbl1 (Proteintech group; 10210-2-AP; polyclonal, lot 00045851)
Snf2h (Abcam; ab3749; polyclonal, lot GR3246671-1)

Peak calling parameters	Read mapping: \$STAR --runMode alignReads --runThreadN 1 --genomeDir \$genome --genomeLoad NoSharedMemory --readFilesIn \$fq1 \$fq2 --readFilesCommand zcat --outFileNamePrefix \$sample. --outSAMtype BAM SortedByCoordinate --outBAMcompression 6 --outFilterMultimapNmax 1 --outFilterMismatchNoverLmax 0.06 --outFilterMatchNmin 40 --outFilterMatchNminOverRead 0.1 --outFilterScoreMinOverRead 0.1 --seedSearchStartLmax 15 --alignIntronMax 1 --alignEndsType Local Peak calling: macs2 callpeak --outdir \$dirName -t \$bedTrt -c \$bedsCtl -f BED -n \$macsOut -g mm -p 1e-2 -m 5 50 --keep-dup all --call-summits --nomodel --extsize 200
Data quality	Reads uniquely mapped to the genome were used. PCR duplicated reads were removed from the alignment. Number of peaks (peak calling: > 5 fold enrichment): Bhlhe40: 11335 Brg1: 14077 Chd4: 25574 Ets1: 14943 IRF4: 9526 cJun: 13263 NFATC1: 5375 Runx1: 34668 Rvb1: 24199 Snf2h: 31186 T-bet: 7642 TCF1: 24772
Software	Sequencing reads were aligned using STAR v2.5.0c. Peaks were called by MACS2 v2.1.1. Peak reproducibility was estimated by IDR v2.0.3. Custom code is available at http://cbio.mskcc.org/public/Leslie/zhongy/downloads/index8.html

Flow Cytometry

Plots

Confirm that:

- The axis labels state the marker and fluorochrome used (e.g. CD4-FITC).
- The axis scales are clearly visible. Include numbers along axes only for bottom left plot of group (a 'group' is an analysis of identical markers).
- All plots are contour plots with outliers or pseudocolor plots.
- A numerical value for number of cells or percentage (with statistics) is provided.

Methodology

Sample preparation	Single cell suspensions of spleens were prepared in ice-cold cell isolation buffer (PBS with 2mM EDTA and 1% FCS) and subjected to red blood cell lysis using ACK buffer (150mM NH4Cl, 10mM KHCO3, 0.1mM Na2EDTA, pH7.3). T cells were enriched using Dynabeads FlowComp mouse CD4 and CD8 kits, according to manufacturer's protocol.
Instrument	Flow Cytometry: LSR II (BD Biosciences), Cell Sorting: Aria II (BD Biosciences)
Software	FACS Diva v8.0 for collection, Flowjo 10.7.1 for analysis.
Cell population abundance	Purification by sorting was performed using FACS Aria II cell sorter (BD Biosciences). Post-sort purity was routinely analyzed and >95%
Gating strategy	Live lymphocytes were gated using FSC-A and SSC-A. Doublets were excluded using FSC-H/FSC-W and SSC-H/SSC-W. CD4 and CD8 T cells were identified as TCRb+ CD4+ and TCRb+ CD8+, respectively. Naive T cells were identified as CD44-CD62L+ cells in uninfected mice. Activated T cells used for CUT&RUN were identified as CD44+ cells in LCMV infected mice. Virus-specific activated and memory T cells were identified using tetramer staining as described in the manuscript.

Tick this box to confirm that a figure exemplifying the gating strategy is provided in the Supplementary Information.